



LUND UNIVERSITY

Improvements in brain imaging using spectral computed tomography: Development and evaluation of novel techniques

Fransson, Veronica

2025

Document Version:

Publisher's PDF, also known as Version of record

[Link to publication](#)

Citation for published version (APA):

Fransson, V. (2025). *Improvements in brain imaging using spectral computed tomography: Development and evaluation of novel techniques*. [Doctoral Thesis (compilation), Department of Translational Medicine]. Lund University, Faculty of Medicine.

Total number of authors:

1

General rights

Unless other specific re-use rights are stated the following general rights apply:

Copyright and moral rights for the publications made accessible in the public portal are retained by the authors and/or other copyright owners and it is a condition of accessing publications that users recognise and abide by the legal requirements associated with these rights.

- Users may download and print one copy of any publication from the public portal for the purpose of private study or research.
- You may not further distribute the material or use it for any profit-making activity or commercial gain
- You may freely distribute the URL identifying the publication in the public portal

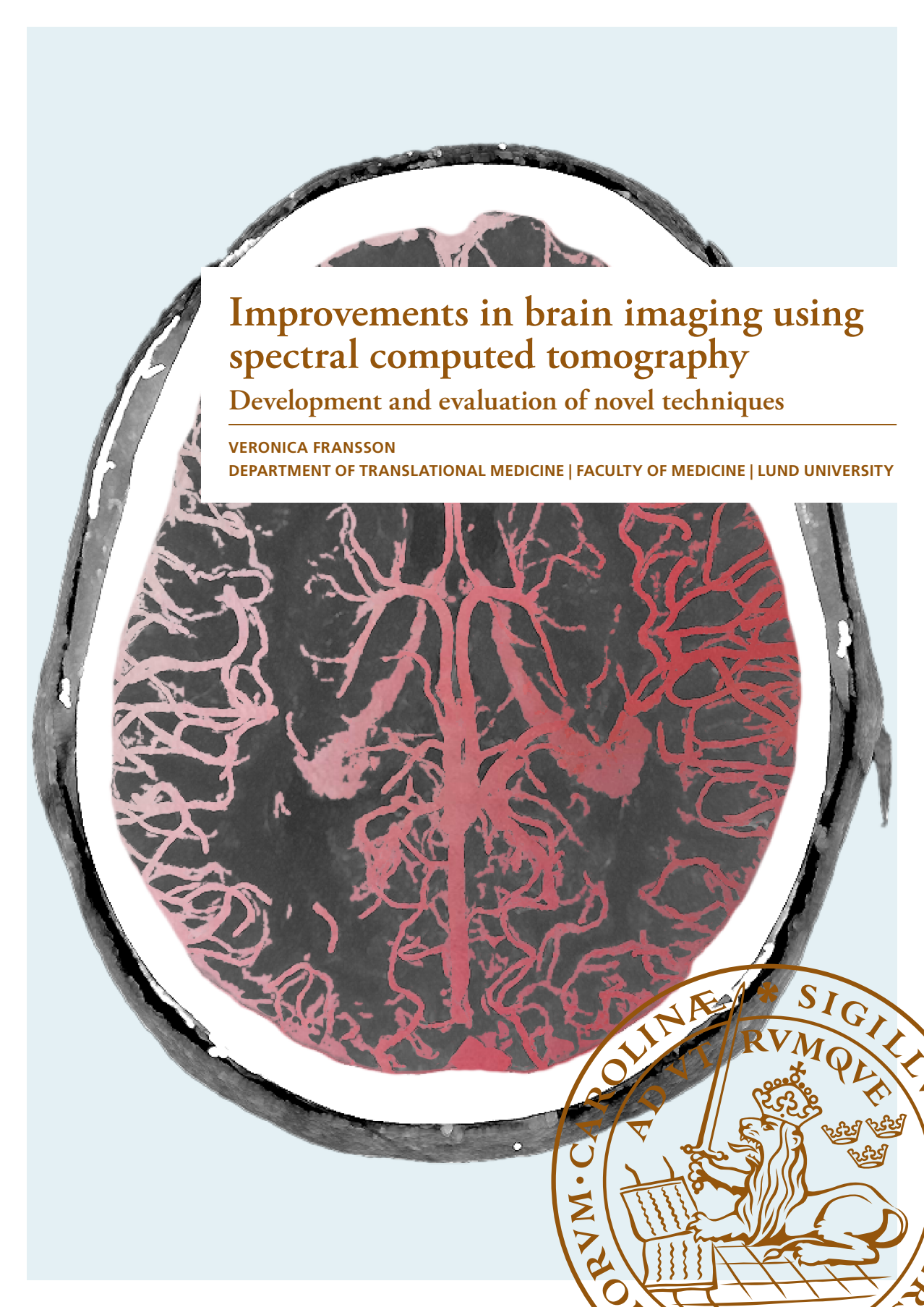
Read more about Creative commons licenses: <https://creativecommons.org/licenses/>

Take down policy

If you believe that this document breaches copyright please contact us providing details, and we will remove access to the work immediately and investigate your claim.

LUND UNIVERSITY

PO Box 117
221 00 Lund
+46 46-222 00 00



Improvements in brain imaging using spectral computed tomography

Development and evaluation of novel techniques

VERONICA FRANSSON

DEPARTMENT OF TRANSLATIONAL MEDICINE | FACULTY OF MEDICINE | LUND UNIVERSITY



Improvements in brain imaging using spectral computed tomography
Development and evaluation of novel techniques

Improvements in brain imaging using spectral computed tomography

Development and evaluation of novel techniques

Veronica Fransson



LUND
UNIVERSITY

DOCTORAL DISSERTATION

Doctoral dissertation for the degree of Doctor of Philosophy (PhD) at the Faculty of Medicine at Lund University to be publicly defended on 28th of May at 13.00 in the Torsten Landberg Lecture Hall, 3rd floor of the Radiotherapy Building, Klinikgatan 5, at Skåne University Hospital in Lund, Sweden.

Faculty opponent

Professor Håkan Geijer

Örebro University Hospital, Örebro University, Sweden

Organization: Medical Radiation Physics, Faculty of Medicine, Lund University

Document name: Doctoral dissertation, Series 2025:60 **Date of issue** 2025-05-28

Author: Veronica Fransson

Sponsoring organization:

Title and subtitle: Improvements in brain imaging using spectral computed tomography – Development and evaluation of novel techniques

Abstract:

Background and aim

Stroke is a life-threatening condition requiring timely and accurate treatment. Computed tomography (CT) is widely used to detect stroke due to its accessibility, speed and diagnostic value. Spectral CT, the latest advancement in CT technology, utilizes multiple energy levels to improve tissue contrast and material differentiation. This thesis aims to evaluate how spectral reconstructions – monoenergetic images (MI) and iodine quantification – can improve brain imaging for stroke assessment.

Methods

Paper I assessed the feasibility of multiphase CT angiography (mCTA) for quantitative brain perfusion analysis, using CT perfusion (CTP) as the reference standard. Paper II compared the diagnostic performance of MIs and conventional polyenergetic images (PI) for detecting ischemia using non-contrast CT (NCCT). Paper III assessed whether contrast media (CM) dose during CTA could be reduced by 50% while maintaining the same image quality as using PIs with a standard CM dose. Paper IV evaluated the effectiveness of using metal artifact reduction (MAR) and MIs to reduce metal artifacts from intracranial coils. All studies were retrospective and, except for Paper I, included both quantitative and qualitative analysis.

Results

Paper I: mCTA demonstrated potential for perfusion deficit detection, with MIs at 40 keV and iodine quantification providing better separation between normal and underperfused tissue than PIs. Paper II: MIs reconstructed at 50–60 keV improved ischemia detection and diagnostic accuracy compared to PIs. Paper III: MIs reconstructed at 50 keV can be used to preserve image quality while reducing CM dose by 50%. With CM dose at 100%, using MIs improved image quality compared to PIs and can be used to salvage scans with poor contrast enhancement. Paper IV: High-energy MIs (≥ 120 keV) with MAR reduced metal artifacts, though lower-energy MIs (60–100 keV) were superior for soft tissue contrast. An intermediate level of 80 keV could provide an optimal balance.

Conclusions

Spectral CT improves stroke imaging by enhancing perfusion assessment, soft tissue contrast, ischemia detection and vascular visualization, and reducing metal artifacts.

Key words: computed tomography, spectral CT, neuroradiology, stroke imaging

Classification system and/or index terms (if any)

Supplementary bibliographical information

Language: English

Number of pages: 94

ISSN and key title: 1652-8220

ISBN: 978-91-8021-713-2

Recipient's notes

Price

Security classification

I, the undersigned, being the copyright owner of the abstract of the above-mentioned dissertation, hereby grant to all reference sources permission to publish and disseminate the abstract of the above-mentioned dissertation.

Signature:

Date: 2025-05-28

Improvements in brain imaging using spectral computed tomography

Development and evaluation of novel techniques

Veronica Fransson



LUND
UNIVERSITY

Coverphoto by Veronica Fransson
Copyright pp 1-94 Veronica Fransson

Paper 1 © Wolters Kluwer Health, Inc. Reproduced with permission. All rights reserved.
Paper 2 © Open Access.
Paper 3 © Open Access.
Paper 4 © The Authors (Manuscript unpublished)

Medical Radiation Physics,
Department of Translational Medicine,
Faculty of Medicine, Lund University, Sweden

ISBN 978-91-8021-713-2
ISSN 1652-8220

Printed in Sweden by Media-Tryck, Lund University
Lund 2025



Media-Tryck is a Nordic Swan Ecolabel
certified provider of printed material.
Read more about our environmental
work at www.mediatryck.lu.se

MADE IN SWEDEN 

“Just as soon as you attain to one ambition you see another one glittering higher up still. It does make life so interesting.”

L.M. Montgomery, Anne of Green Gables

Table of Contents

List of papers	10
List of contributions	11
Related papers not included in this thesis	11
Thesis at a glance.....	12
Abstract	13
Populärvetenskaplig sammanfattning.....	14
Abbreviations	16
Declaration of generative artificial intelligence usage.....	17
Introduction.....	19
Rationale	20
Research aims	20
Background.....	21
Computed tomography physics	21
Photon interaction with matter.....	22
Spectral computed tomography	24
Material decomposition	27
Material-specific images	29
Monoenergetic images	30
Image quality.....	32
Noise	32
Contrast resolution	33
Artifacts	34
Diagnostic performance.....	36
Visual grading analysis	38
Neuroradiology	42
Stroke imaging.....	42
Artifacts in brain imaging	44
Differentiation of gray and white matter	45

Contrast medium.....	46
Radiation dose and associated risks	47
Radiation dose in CT imaging	48
Summary of the studies	51
Data collection	51
Ethical considerations	52
Statistical methods.....	52
Paper I.....	52
Paper II	56
Paper III.....	58
Paper IV	59
Results and discussion	63
Contributions to stroke imaging.....	63
Brain perfusion	63
Differentiation of gray and white matter	65
Diagnostic performance.....	66
Arterial enhancement.....	67
Salvaging examinations with poor arterial enhancement.....	70
Artifacts in brain imaging	71
Signal-to-noise ratio.....	74
Contrast-to-noise ratio	75
Radiation dose considerations.....	75
Limitations.....	76
Conclusions	79
Future perspectives.....	81
Författarens tack	82
References	85

List of papers

This thesis is based on the following papers, which will be referred to in the thesis by their Roman numerals, I-IV. The papers are appended at the end of the thesis.

- I. **Detection of Perfusion Deficits in Multiphase Computed Tomography Angiography—A Stroke Imaging Technique Based on Iodine Mapping on Spectral Computed Tomography: Initial Findings**
Fransson V, Mellander H, Wassélius J, Ydström K
Journal of Computer Assisted Tomography. 2021. 45(4):618–624.
- II. **Virtual monoenergetic images by spectral detector computed tomography may improve image quality and diagnostic ability for ischemic lesions in acute ischemic stroke**
Mellander H, Bengtsson P, Fransson V, Ramgren B, Undrén P, Drake M, Ydström K, Lätt J, Hilal A, Wassélius J, Ullberg T
Acta Radiologica. 2023. 64(4):1631–1640
- III. **Image quality of spectral brain computed tomography angiography using halved dose of iodine contrast medium**
Fransson V, Mellander H, Ramgren B, Andersson H, Arena F, Ydström K, Ullberg T, Wassélius J
Neuroradiology. 2023. 65:1333–1342
- IV. **Metal artifact reduction and monoenergetic imaging: Effects on brain visualization in photon counting and dual layer computed tomography**
Fransson V, Andersson H, Mellander Oxholm H, Ramgren B, Wassélius J, Tingberg A, Ydström K
Manuscript

Paper I was reproduced with kind permission by Wolters Kluwer.

Papers II-III were published with open access.

List of contributions

Below is a summary of my contributions to each of the original papers:

- I. I was the primary contributor to the study design and development of the methodology. I planned and conducted all measurements, analyzed the data and authored and revised the manuscript as the main and corresponding author.
- II. I contributed to the development of the methodology and the setup for the qualitative data collection. I took part in interpreting the results and editing of the manuscript. Helena Mellander Oxholm was the leading PhD student on the project.
- III. I worked on this project alongside PhD student Helena Mellander Oxholm, taking equal part in the study design and development of the methodology. I planned and conducted all measurements, analyzed the data and authored and revised the manuscript as the main author.
- IV. I was the primary contributor to the study design and development of the methodology. I planned and conducted all measurements, analyzed the data and authored the manuscript as the main and corresponding author.

Related papers not included in this thesis

Metal artifact reduction by virtual monoenergetic reconstructions from spectral brain CT

Mellander H, Fransson V, Ydström K, Lätt J, Ullberg T, Wassélius J, Ramgren B
European Journal of Radiology Open. 2023. 10:100479.

Deep learning volumetric brain segmentation based on spectral CT

Fransson V, Christensen S, Ydström K, Wassélius J
In Medical Imaging 2023: Physics of Medical Imaging. 2023;1246336. (Progress in Biomedical Optics and Imaging – Proceedings of SPIE).

Thesis at a glance

Study	Question	Method	Results and Conclusions
I	Can quantitative measurements in multi-phase CT angiography differentiate normal from underperfused regions?	Quantitative analysis of iodine concentration and HU ^A in PI ^B and MI ^C (40 keV) reconstructions of patient images (n=5 with underperfusion, n=5 without) in vascular regions.	The ratio of iodine concentration or HU between hemispheres can indicate underperfusion. Iodine and MIs (40 keV) provided greater differentiation than PIs.
II	Can MIs reconstructed from brain CTs enhance detection of acute ischemic lesions compared to PIs?	Quantitative and qualitative analysis of PI and MI (40-200 keV) reconstructions of patient images (n=29 with ischemic lesions, n=23 without).	Low-energy MIs (40-70 keV) improved contrast between ischemic gray and normal white matter. Access to MIs may increase the sensitivity for detecting acute ischemia.
III	Can MIs reconstructed from brain CT angiography enable a 50% reduction in contrast medium dose while maintaining image quality? Can MI salvage examinations with poor timing?	Quantitative and qualitative analysis of PI and MI reconstructions of patient images (n=55 with 100% dose, n=43 with 50% dose, n=29 with 50% dose and poor timing).	Low-energy MIs (50 keV) with 50% reduced contrast medium may provide better image quality than PIs with 100% dose, and can be used to salvage poorly timed examinations, thus reducing the number of non-diagnostic examinations.
IV	How does combining of MIs reconstructed from brain CTs with MAR ^D impact artifact severity and soft tissue contrast of intracranial tissues?	Quantitative and qualitative analysis of PIs and MIs, with and without MAR, for a phantom (with and without metal coils) and a patient (with coils).	High-energy MIs (120-140 keV) combined with MAR minimized artifacts, while lower-energy MIs (60 keV) optimized soft tissue contrast. MIs at 80 keV could provide an optimal balance.

^AHounsfield Units (HU)

^BPolyenergetic Image (PI)

^CMonoenergetic Image (MI)

^DMetal Artifact Reduction (MAR)

Abstract

Background and aim

Stroke is a life-threatening condition requiring timely and accurate treatment. Computed tomography (CT) is widely used to detect stroke due to its accessibility, speed and diagnostic value. Spectral CT, the latest advancement in CT technology, utilizes multiple energy levels to improve tissue contrast and material differentiation. This thesis aims to evaluate how spectral reconstructions – monoenergetic images (MI) and iodine quantification – can improve brain imaging for stroke assessment.

Methods

Paper I assessed the feasibility of multiphase CT angiography (mCTA) for quantitative brain perfusion analysis, using CT perfusion (CTP) as the reference standard. **Paper II** compared the diagnostic performance of MIs and conventional polyenergetic images (PI) for detecting ischemia using non-contrast CT (NCCT). **Paper III** assessed whether contrast media (CM) dose during CTA could be reduced by 50% while maintaining the same image quality as using PIs with a standard CM dose. **Paper IV** evaluated the effectiveness of using metal artifact reduction (MAR) and MIs to reduce metal artifacts from intracranial coils. All studies were retrospective and, except for Paper I, included both quantitative and qualitative analysis.

Results

Paper I: mCTA demonstrated potential for perfusion deficit detection, with MIs at 40 keV and iodine quantification providing better separation between normal and underperfused tissue than PIs. **Paper II:** MI reconstructed at 50–60 keV improved ischemia detection and diagnostic accuracy compared to PIs. **Paper III:** MIs reconstructed at 50 keV can be used to preserve image quality while reducing CM dose by 50%. With CM dose at 100%, using MIs improved image quality compared to PIs and can be used to salvage scans with poor contrast enhancement. **Paper IV:** High-energy MIs (≥ 120 keV) with MAR reduced metal artifacts, though lower-energy MIs (60–100 keV) were superior for soft tissue contrast. An intermediate level of 80 keV could provide an optimal balance.

Conclusions

Spectral CT improves stroke imaging by enhancing perfusion assessment, soft tissue contrast, ischemia detection and vascular visualization, and reducing metal artifacts.

Populärvetenskaplig sammanfattning

Stroke är ett livshotande tillstånd som uppstår på grund av av syrebrist i hjärnan, orsakat av en blodpropp eller blödning. 2 miljoner hjärnceller dör varje minut, så för att minska risken att patienten får bestående skador, eller i värsta fall avlider, är en snabb diagnos och behandling nödvändig för att återställa blodflödet.

Datortomografi (DT) är en avancerad röntgenteknik som är central vid stroke-diagnostik. I DT-undersökningar så roterar röntgenröret runt patienten och producerar röntgenstrålning som skickas genom kroppen. Röntgenstrålning består av ett spektrum av energier, vilket påverkar hur den interagerar med vävnaden och hur DT-bilden ser ut. Röntgenstrålningen som passerar kroppen fångas upp av en detektor och används för att skapa bilder av kroppens inre. Kroppens vävnader attenuerar, med andra ord dämpar, strålningen olika mycket beroende på materialsammansättning. Material med hög attenuering (till exempel skelett) är ljusa i DT-bilden, medan material med låg attenuering (till exempel lungor) är mörka. Alla material däremellan, som fett och muskler, visas i en gråskalenyans någonstans mellan svart och vitt. DT-bilder är detaljerade tvärsnittsbilder, som ger bättre visualisering än vanlig, så kallad slät, röntgen där vävnader visas överlagrade på varandra.

Ett problem med konventionell DT är att olika vävnader kan ha liknande attenuering vilket gör dem omöjliga att särskilja i bilden. För cirka 20 år introducerades spektral DT, som löser detta genom att utnyttja att vävnader attenuerar röntgenstrålningen olika mycket beroende på röntgenstrålarnas energi. Genom att ta bilder vid två eller flera energier kan man skapa bilder som förstärker kontrasten mellan vävnader med liknande attenuering. En viktig tillämpning är monoenergetiska bilder, som modellerar hur bilden skulle ha sett ut om den skapats med röntgenstrålar av en enda energi. Med spektral CT kan också materialspecifika bilder skapas, till exempel jodkartor som visar kontrastmedelsupptag. Kontrastmedel, ofta jod-baserade på grund av jods höga attenuering, används till exempel för att kunna se blodkärl, som annars är "osynliga" i röntgenbilden eftersom de har samma attenuering som sin omgivning. Men genom att injicera kontrastmedel i blodomloppet kan de synliggöras.

Vid misstänkt stroke görs flera DT-undersökningar. Först görs en hjärnundersökning utan kontrastmedel för att bedöma hjärnvävnaden. Därefter görs undersökningar med kontrastmedel för att bedöma hjärnans blodförsörjning. DT angiografi används för att visuellt utvärdera blodkärlen och identifiera blodproppar. DT perfusion används för att matematiskt analysera hjärnans blodförsörjning och identifiera områden med syrebrist. Utifrån dessa undersökningsresultat bestämmer läkare vilken behandling som bör ge patienten den bästa chansen till återhämtning.

Avhandlingens syfte är att undersöka hur spektral DT kan förbättra stroke-diagnostiken, genom att utveckla nya metoder och utvärdera hur monoenergetiska bilder och jodkartor kan användas för att förbättra undersökningskvaliteten.

I den första studien undersöktes om kvantitativ analys av DT angiografi kan ge samma information som DT perfusion. Resultaten indikerade att det går, men metoden behöver vidare utveckling. Vi såg även att monoenergetiska bilder och jodkartor förstärkte skillnaden mellan frisk och skadad vävnad, vilket skulle kunna medföra en högre detektion av ischemi, jämfört DT perfusion som är baserad på konventionella DT-bilder.

Vävnad skadad på grund av en blodpropp kan identifieras genom att hitta områden med en förlorad kontrast mellan grå och vit hjärnsubstans. Den andra studien utvärderade om monoenergetiska bilder kan förbättra upptäckten av dessa skador i DT-bilder utan kontrastmedel. Studien visade att den diagnostiska förmågan – d.v.s. antalet korrekt identifierade skador – förbättrades när granskande läkare hade tillgång till monoenergetiska bilder.

Eftersom jodbaserat kontrastmedel kan ge en ökad risk för njurskador, och har en negativ miljöpåverkan, undersökte den tredje studien om kontrastdosen kan halveras i DT angiografi genom att använda monoenergetiska bilder. Resultaten visade att det inte bara var möjligt – utan att bildkvaliteten kunde förbättras jämfört med konventionella bilder och full kontrastdos. Studien visade också att monoenergetiska bilder kan rädda undersökningar där bildtagningens timing blivit fel, vilket annars kan försämra diagnostiken eller leda till omtag – som medför extra strålning och kontrastmedel för patienten.

Patienter har i vissa fall metallimplantat i hjärnan, vilket skapar störningar (s.k. artefakter) i DT-bilden. I den fjärde studien utvärderades hur kombinationen monoenergetiska bilder och mjukvaror för metallartefaktsreduktion påverkar bildkvaliteten i DT-bilder utan kontrastmedel. Resultaten visade att mjukvaran för metallartefaktsreduktion var mer betydelsefullt än energinivån hos de monoenergetiska bilderna för att minska artefakter, men mjukvaran kunde också introducera nya artefakter. Höga monoenergetiska bilder med metallartefaktsreduktion gav minst störningar. Låga monoenergetiska bilder medförde en bättre mjukvävnadskontrast och föredrogs därför av de granskande läkarna, trots att mängden artefakter ökade.

Sammanfattningsvis visar avhandlingen att spektral DT kan förbättra både stroke-diagnostik och den bredare neuroradiologin. Spektral DT medför möjlighet till nya och förbättrade metoder för bedömning av blodförsörjning, förbättrad detektion av stroke, reducerad kontrastmedelsanvändning och mindre störningar från metallimplantat.

Abbreviations

A	Atomic mass
AHARA	As High As Reasonably Achievable
AI	Artificial Intelligence
ALARA	As Low As Reasonably Achievable
AUC	Area Under Curve
AUC _{VGC}	Area Under the Visual Grading Characteristics Curve
CBF	Cerebral Blood Flow
CBV	Cerebral Blood Volume
CIN	Contrast-induced Nephropathy
CM	Contrast Medium
CNR	Contrast-to-Noise Ratio
CT	Computed Tomography
CTA	Computed Tomography Angiography
CTDI	Computed Tomography Dose Index
CTDI ₁₀₀	Computed Tomography Dose Index (averaged over 100 mm)
CTDI _{vol}	Computed Tomography Dose Index (volumetric)
CTDI _w	Computed Tomography Dose Index (weighted)
CTP	Computed Tomography Perfusion
DECT	Dual Energy Computed Tomography
DLCT	Dual Layer Computed Tomography
DLP	Dose Length Product
DNA	Deoxyribonucleic Acid
DSCT	Dual Source Computed Tomography
FN	False Negatives
FP	False Positives
FPF	False Positive Fraction
HU	Hounsfield Units
ICA	Internal Carotid Artery
ICRP	International Commission on Radiological Protection
ID	Iodine Density
LNT	Linear-No-Threshold
M2	M2-segment of the Middle Cerebral Artery
MAR	Metal Artifact Reduction
MCA	Middle Cerebral Artery

mCTA	Multiphase Computed Tomography Angiography
MI	Monoenergetic Image
MRI	Magnetic Resonance Imaging
MTT	Mean Transit Time
MVD	Maximum Value of Derivative
NCCT	Non-Contrast Computed Tomography
NPS	Noise Power Spectrum
NPV	Negative Predictive Value
PCCT	Photon Counting Computed Tomography
PET	Positron Emission Tomography
PMMA	Polymethyl Methacrylate
PI	Polyenergetic Image
PPV	Positive Predictive Value
ROC	Receiver Operator Characteristics
SD	Standard Deviation
SNR	Signal-to-Noise Ratio
SSDE	Size Specific Dose Estimate
Tmax	Time to Maximum contrast enhancement
TN	True Negative
TNF	True Negative Fraction
TP	True Positive
TPF	True Positive Fraction
VGA	Visual Grading Analysis
VGC	Visual Grading Characteristics
VNC	Virtual Non Contrast
Z	Atomic Number

Declaration of generative artificial intelligence usage

This thesis has in part been produced with the assistance of generative artificial intelligence (AI) models (GPT-4 by OpenAI) mainly to improve language and readability. I, the author, have processed the generated text and take full responsibility for the content.

Introduction

Computed tomography (CT) is an indispensable diagnostic imaging modality thanks to its high accessibility, speed of image acquisition and diagnostic value. In recent years, spectral CT solutions have been developed to enhance the contrast between different materials or tissue, making it easier to differentiate between them. With spectral CT, image data are acquired at two or more X-ray energy levels, enabling material decomposition (the separating of different materials based on how they absorb X-rays at different energy levels) and reconstruction (converting the X-ray data into cross-sectional images of the body) of synthetic monoenergetic images (MI). For many diagnostic situations, high contrast is required for distinguishing between types of soft tissue, such as in the identification of ischemic stroke. Compared to a conventional CT image, MI reconstructed at an energy level lower than the mean energy of the X-ray spectrum may enhance soft tissue contrast. Spectral CT enables multiple new image reconstructions, but to avoid irrelevant information and minimize radiologist workload, the optimal reconstruction for each diagnostic task needs to be determined. The medical profession has an obligation to use resources as effectively as possible, making sure that as many patients as possible can receive the care they need.

In diagnostic imaging, there are many variables to consider when optimizing images: image quality, system capability and strengths, radiation dose and contrast medium concentration and dose, to name a few. At the core of image optimization is ALARA, “*as low as reasonably achievable*”, while maintaining AHARA, “*as high as reasonably achievable*”, meaning that the image or examination quality should be as high as possible, but the radiation dose (or risk of negative effects) cannot be higher than that required to enable a correct diagnosis.

Stroke is a life-threatening condition, with a high risk of permanent neurological damage, and its incidence is projected to increase as the global population ages [1]. To minimize the damage, correct and timely treatment is of the essence. As such, high quality diagnostic brain imaging is crucial. In this thesis, the focus was specifically on neuroradiological examinations typical for stroke imaging, to determine whether and how they can benefit from spectral imaging.

Rationale

The motivation behind this thesis was to explore neuroradiological applications of spectral CT to increase and optimize its use and leverage its full potential.

Research aims

The overarching aim of this thesis was to explore how spectral CT, particularly monoenergetic and iodine imaging, can enhance neuroradiologic examinations of the brain.

The specific aims for each paper were:

- I. To develop and evaluate a novel method for differentiating brain tissue (distinguishing underperfused from normal tissue, with conventional CT perfusion as reference) in multiphase CT angiography, on a dual layer CT, using MI and iodine quantification.
- II. To assess whether MI improves the detection of acute cortical ischemic lesions in non-contrast brain CT, on a dual layer CT, compared to conventional polyenergetic images (PI).
- III. To investigate the feasibility of reducing contrast medium (CM) dose by 50% in brain CT angiography, on a dual layer CT, without compromising image quality, and to evaluate whether MI can salvage examinations with suboptimal contrast medium timing.
- IV. To examine the combined effects of MI and metal artifact reduction algorithms on artifact severity and soft tissue contrast in non-contrast brain CT with intracranial metal, using both dual layer CT and photon counting CT.

Background

In 1957, Allan M. Cormack laid the theoretical foundation for CT, while Godfrey N. Hounsfield developed the first CT scanner between 1966 and 1972 [2]. The first CT prototype, tested in 1971, immediately revolutionized medical X-ray technology. Unsurprisingly, Cormack and Hounsfield were jointly awarded the Nobel prize in Physiology or Medicine in 1979 for their ground-breaking innovation.

Since the 1970s, CT technology has made tremendous advancements and has solidified its position at the forefront of diagnostic imaging [3]. Increased volume coverage, made possible by helical data acquisition and multi-slice detectors, combined with higher temporal resolution through faster gantry rotation, larger helical pitch and dual X-ray tube data acquisition, has made more advanced and dynamic imaging possible. Another milestone was the addition of spectral information. Although the dual energy CT (DECT) concept dates back to the advent of the first CT, its practical realization required extensive advancements in software and hardware. The first clinically available DECT system was introduced in 2006 [4, 5]. In 2022, CT imaging was revolutionized once again with the introduction of the first clinical photon counting CT [6, 7]

Computed tomography physics

A conventional CT scanner contains an X-ray tube and a detector. These are situated opposite each other on a gantry, which rotates around the patient. Photons emitted by the X-ray tube are either absorbed or scattered by the patient's body (attenuated) or pass through and are captured by the detector, where they produce a signal proportional to their energy. When a photon is attenuated in the patient, part of or all of its energy is deposited. The deposited energy leads to the patient absorbing a radiation dose, with potentially damaging effects to the irradiated tissue.

The linear attenuation coefficient (μ) describes the probability of photon attenuation when travelling through a material and is dependent on both the photon energy and material properties (density and atomic number). The attenuation of a photon beam, where every photon has the same energy, through an arbitrary material is expressed by:

$$I = I_0 e^{-\mu x} \quad (1)$$

where I is the intensity (number of photons) of the photon beam after having travelled x cm in the material, I_0 is the initial intensity and μ [cm^{-1}] the linear attenuation coefficient of the material at the specific photon energy. An X-ray tube produces photons with a spectrum of energies and tissue is composed of many different materials, making the reality much more complicated – but the principle for attenuation stays the same.

The photons that are captured by the detector generate projection data which are processed and rendered into cross-sectional CT images through tomographic reconstruction. From the tomographic reconstruction, the average linear attenuation coefficient of each voxel (a three-dimensional counterpart to a pixel) is calculated. Rather than presenting the image directly, the linear attenuation coefficient is converted to CT-numbers, expressed in Hounsfield units (HU), by relating the attenuation in each voxel to the linear attenuation coefficients of water and air:

$$HU = k \cdot \frac{\mu_{\text{object}} - \mu_{\text{water}}}{\mu_{\text{water}} - \mu_{\text{air}}} \quad (2)$$

where $k=1000$ and μ_{water} and μ_{air} are the linear attenuation coefficients of water and air respectively. By definition, water has a CT-number of 0 HU, and air -1000 HU. Images are presented in grayscale, where HU values are assigned to shades of gray ranging from black (-1000 HU) to white (+1000 HU). Since human vision is incapable of discriminating between 2000 shades of gray, windowing techniques are generally used to highlight certain tissues, rather than viewing the image in the full range of HU [8].

Photon interaction with matter

Diagnostic CT is performed using X-ray tube voltages of 70-150 kV, producing an X-ray spectrum with mean energies of 40-70 keV. In this energy range, photon interact with matter in different ways. These interaction mechanisms include the photoelectric effect, Compton (incoherent) scattering and Rayleigh (coherent) scattering.

The photoelectric effect is a process in which a photon interacts with an electron from an atom, resulting in the total absorption of the photon and the electron being ejected from the atom. Compton scattering also results in an electron being ejected from the atom, but the photon is not absorbed. Instead, it changes direction, losing part of its energy in the process. Rayleigh scattering is similar to Compton scattering, but no electron is ejected in the process.

The mass attenuation coefficient (μ/ρ) is the linear attenuation coefficient (μ) normalized by density (ρ), creating a value which is constant for each material (although varying with energy). The total mass attenuation coefficient is expressed by the sum of the mass attenuation coefficients for each interaction mechanism:

$$\left(\frac{\mu}{\rho}\right) = \left(\frac{\mu}{\rho}\right)_{\text{Photoelectric}} + \left(\frac{\mu}{\rho}\right)_{\text{Compton}} + \left(\frac{\mu}{\rho}\right)_{\text{Rayleigh}} \quad (3)$$

The contribution of Rayleigh (coherent) scatter can be considered negligible, simplifying the equation to include only the mass attenuation coefficients of the photoelectric effect and Compton scattering (Figure 1).

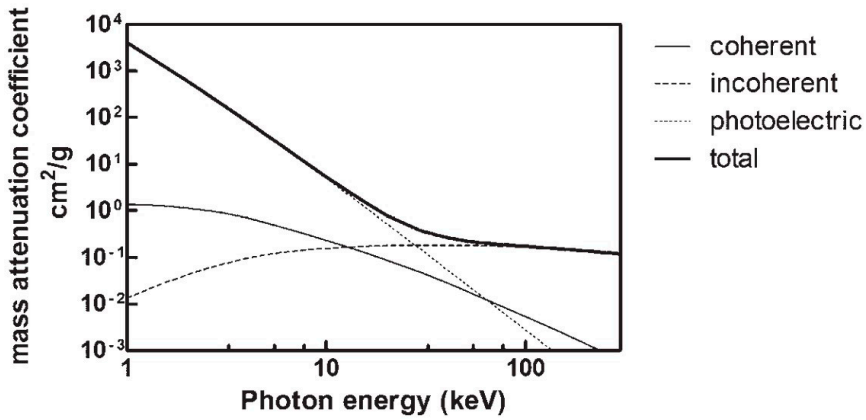


Figure 1.

Mass attenuation coefficients of water for Rayleigh (coherent) scattering, Compton (incoherent) scattering, photoelectric effect and the total mass attenuation coefficient, for photon energies ranging from 1 to 300 keV [9].

The mass attenuation coefficient for photoelectric absorption is dependent on the material and energy, as described by [10]:

$$\left(\frac{\mu}{\rho}\right)_{\text{Photoelectric}} \propto \frac{Z^4}{(\text{keV})^{7/2}} \quad (4)$$

where Z is the atomic number (or effective atomic number, which is used to describe the average atomic number for human tissue as it is composed of multiple elements), and keV denotes the photon energy.

The photoelectric effect is the dominating attenuation mechanism in soft tissues at low photon energies (below 26 keV) [11]. K-edges correspond to abrupt increases in the

probability of the photoelectric effect, occurring when the photon energy matches the binding energy of electrons in an atom's inner shell. The phenomenon is particularly notable in materials with high effective atomic number, as their K-edges fall within the diagnostic X-ray spectrum. As photon energy increases, the photoelectric effect becomes less dominant, except at K-edges, and Compton scattering becomes increasingly important. The mass attenuation coefficient for Compton scattering, in the diagnostic CT energy range, has the following dependence:

$$\left(\frac{\mu}{\rho}\right)_{Compton} \propto \frac{Z}{A} \quad (5)$$

where A is the effective atomic mass. Most soft tissues have a similar $\frac{Z}{A}$ ratio.

In the diagnostic CT energy range, photon energies are high enough to make Compton scattering 10 times more probable than the photoelectric effect for soft tissue. The photoelectric effect, however, contributes more to the attenuation of materials containing elements with a higher atomic number, such as bone, metal and iodinated CM.

In summary, attenuation increases with increasing atomic number and material density but decreases with increasing photon energy, except at K-edges.

Spectral computed tomography

Since photon attenuation, measured by the linear attenuation coefficient, is dependent on both atomic number and material density, different materials can have the same HU value, making it challenging, or impossible, to differentiate between them in CT images. However, acquiring an additional CT scan at a second X-ray energy can improve differentiation.

Spectral CT is used to describe CT systems capable of separating the signal from detected photons into two or more energy bins to achieve spectral resolution. These include DECT systems, as well as photon counting CT (PCCT). DECT employs different solutions, including dual layered detectors or dual X-ray sources (Figure 2) [12].

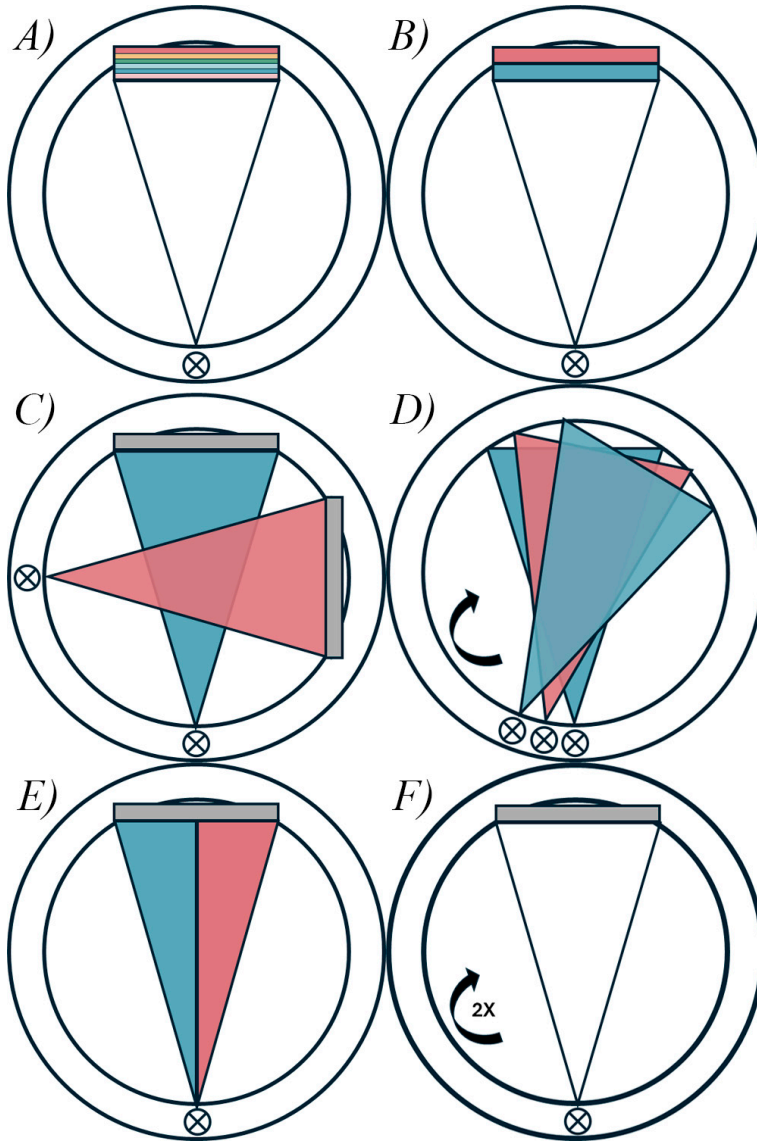


Figure 2.

A) Photon counting computed tomography (CT) with an energy-resolving detector. B) Dual layer CT. C) Dual source CT. D) Rapid kV-switching CT. E) Split-beam CT. F) Dual scan CT. For the dual energy systems in B-F, the blue and red colors represents low and high X-ray energy.

The ability to correctly separate and identify materials in a CT image depends on several factors, including spectral separation (the degree of overlap between the low- and high-energy data sets), temporal coherence (time difference between low- and high-energy data sets), noise levels and the reconstruction algorithm employed [3]. Material

decomposition performed in the projection space (i.e. pre-reconstruction) is theoretically more accurate than image space decomposition (i.e. post-reconstruction), offering the advantage of mitigating beam hardening artifacts [12]. However, the actual difference in performance using one method over the other may not be as large as was previously assumed since many factors in combination affect the result [13].

Ideally, low- and high-energy data sets would be acquired simultaneously, have similar photon counts, minimal noise, and a large spectral separation with no overlap (i.e. resembling two monochromatic beams). Current technology, however, necessitates compromises.

Photon counting CT

PCCT acquires all photons, regardless of energy, simultaneously, enabling material decomposition in the projection space. The semi-conducting detector provides excellent spectral separation thanks to its inherent energy resolution. Electronic noise, primarily found in the lowest energy bins, is eliminated by applying a threshold below which detected photons are discarded before image reconstruction. The first clinically available PCCT employed a cadmium-telluride-based detector [6]. This type of detector can be fabricated with smaller detector elements than scintillator detectors, improving spatial resolution. Furthermore, prototypes using silicon-based detectors, currently under development, may provide even better spectral resolution.

Dual layer CT

Dual layer CT (DLCT), like other conventional energy-integrating detector systems and DECT systems, uses scintillator detectors. Its two-layered detector design allows the top layer to primarily capture low-energy photons, while the bottom layer primarily captures high-energy photons. Spectral overlap occurs as some low-energy photons are detected by the bottom layer and vice versa, due to the stochastic nature of photon attenuation. DLCT has the advantage of simultaneous low- and high-energy data acquisition, allowing material decomposition in the projection space. High- and low-energy data sets are always acquired, but one can choose whether to reconstruct spectral images or combine the data to a conventional PI.

Dual source CT

Dual source CT (DSCT) uses two X-ray tubes positioned 90 degrees apart on a rotating gantry, operating at two different voltages. This setup provides excellent spectral separation, with spectral degradation primarily due to contamination by scattered photons. Applying physical filters to the higher-energy X-ray tube further improves spectral separation. However, as data acquisition is not simultaneous, material

decomposition must be performed in the image space after reconstructing the high- and low- energy images separately. Misalignment between the two images can degrade the accuracy of the material decomposition.

Rapid kV-switching CT

In the rapid kV-switching CT approach, the X-ray tube alternates voltage to generate a high and low energy level approximately every millisecond, enabling near-simultaneous acquisition of the low- and high-energy data. Despite some spectral overlap, this method achieves good spectral resolution.

Split-beam CT

Split-beam CT employs a physical filter to divide the photon beam into two energy ranges. The detector can be either single- or dual-layer, with acquisitions occurring near-simultaneously. The spectral resolution is adequate with a single layer detector but is improved using a dual layer detector.

Dual scan CT

Dual scan CT acquires one scan with low energy, followed by a second scan with high energy. While this method provides excellent spectral separation, the temporal delay between acquisitions introduces a high risk of motion artifacts and misalignment between the data sets.

Material decomposition

Material decomposition is a technique for determining the contribution of specific materials in each voxel of the image by utilizing the energy- and material-dependent nature of photon attenuation [13]. This approach separates attenuation into material- and energy-specific components, making it easier to determine a material's composition from spectral imaging data. Materials without K-edges within the diagnostic imaging energy range have smooth changes in their attenuation with varying energy. The mass attenuation coefficient for any material, at a specific energy E , can be expressed as a linear combination of attenuation by the photoelectric effect and Compton scattering:

$$\left(\frac{\mu}{\rho}\right)(E) = \alpha_P \cdot f_P(E) + \alpha_C \cdot f_C(E) \quad (6)$$

where α_P , α_C are material dependent factors and f_P , f_C energy-dependent factors for the photoelectric effect and Compton scatter, respectively. When attenuation

measurements at two distinct energies (E_{Low} and E_{High}) are available, α_P and α_C can be determined from equations 7 and 8:

$$\left(\frac{\mu}{\rho}\right)(E_{Low}) = \alpha_P \cdot f_P(E_{Low}) + \alpha_C \cdot f_C(E_{Low}) \quad (7)$$

$$\left(\frac{\mu}{\rho}\right)(E_{High}) = \alpha_P \cdot f_P(E_{High}) + \alpha_C \cdot f_C(E_{High}) \quad (8)$$

With the material-dependent factors determined, the attenuation in every voxel, at any energy, can be modelled. This is the principle behind the generation of synthetic MI reconstructions.

Furthermore, the attenuation of any material can be modelled as the linear combination of two basis materials (e.g., water and iodine) [14]:

Two basis materials, 1 and 2, have the following attenuation:

$$\left(\frac{\mu}{\rho}\right)_1 = \alpha_{1,P} \cdot f_P(E) + \alpha_{1,C} \cdot f_C(E) \quad (9)$$

$$\left(\frac{\mu}{\rho}\right)_2 = \alpha_{2,P} \cdot f_P(E) + \alpha_{2,C} \cdot f_C(E) \quad (10)$$

The mass attenuation of a third unknown material, given by equation 6 can, by substitution of $f_P(E)$ and $f_C(E)$ from equation 9 and 10, be expressed as a linear combination of the two basis materials:

$$\left(\frac{\mu}{\rho}\right)_3 = m_1 \cdot \left(\frac{\mu}{\rho}\right)_1(E) + m_2 \cdot \left(\frac{\mu}{\rho}\right)_2(E) \quad (11)$$

where

$$m_1 = \frac{\alpha_{3,P} \cdot \alpha_{2,C} - \alpha_{3,C} \cdot \alpha_{2,P}}{\alpha_{1,P} \cdot \alpha_{2,C} - \alpha_{2,P} \cdot \alpha_{1,C}} \quad (12)$$

and

$$m_2 = \frac{\alpha_{3,C} \cdot \alpha_{1,P} - \alpha_{3,P} \cdot \alpha_{1,C}}{\alpha_{1,P} \cdot \alpha_{2,C} - \alpha_{2,P} \cdot \alpha_{1,C}} \quad (13)$$

Neither a physical effect-model (equation 6) nor a material basis-model (equation 11) are good fits when the K-edge effect is a major contributing source of the attenuation [13]. In cases involving K-edges, three-material decomposition can be used by adding a K-edge term to the mass attenuation expression:

$$\left(\frac{\mu}{\rho}\right)(E) = \alpha_P \cdot f_P(E) + \alpha_C \cdot f_C(E) + \alpha_K \cdot f_K(E) \quad (14)$$

Where α_K and f_K represents the material- and energy-dependence of the K-edge effect. Determination of three materials from only two measurements is made possible by the assumption of volume or mass conservation [15]. If there is more than one K-edge material, two measurements at different energy levels will not be enough to solve the mathematical problem.

Material decomposition can be performed post-reconstruction (image space) or pre-reconstruction (projection space) of the CT image. The above equations refer to material decomposition in the image space, but there are corresponding equations for the projection space approach.

Material-specific images

Material-specific images are derived from spectral CT data by decomposing the material composition in each voxel and displaying the amount or concentration of specific materials. For example, iodine density (ID) maps present the concentration of iodine within a voxel. Iodine is an important element in CT imaging as it is the most common contrast agent, commonly injected intravenously to enable vascular assessment or identify abnormal masses (i.e. tumors). Another example of a material-specific image is uric acid maps. Uric acid is present in kidney stones and these images can aid in kidney stone diagnosis.

Material-specific images of materials with a strong energy-dependence (i.e. attenuation changes more noticeably across different energies) are more accurate than that of materials with a weak energy-dependence. The energy-dependence can be characterized by a dual energy ratio, the ratio of attenuation at high versus low energy, with higher dual energy ratios facilitating the creation of material-specific images. However, the dual energy ratio of a material varies across spectral CT systems, depending on the quality of the spectral separation.

Materials with higher effective atomic numbers exhibits stronger energy dependence) compared to those with lower effective atomic numbers. Most elements making up human tissue, such as hydrogen ($Z=1$), carbon ($Z=6$), nitrogen ($Z=7$) and oxygen ($Z=8$), have low atomic numbers and show relatively similar attenuation across different energies, making it difficult to differentiate between them. In contrast, elements such as calcium ($Z=20$) and iodine ($Z=53$) demonstrate a pronounced energy-dependence caused by their higher atomic numbers, allowing them to be easily distinguished from other elements.

Since the iodine contribution within each voxel can be quantified, it can also be subtracted from the original image to produce a virtual non-contrast (VNC) image. VNC images can potentially replace true non-contrast images, reducing the number of scans and lowering radiation dose. Additionally, VNC images are useful for differentiating contrast medium extravasation from hemorrhage.

Monoenergetic images

MIIs simulate the attenuation properties of a monochromatic X-ray beam at a specified energy level, derived from spectral CT data (Figure 3). These images are generated by modelling the attenuation of each voxel based on the calculated contributions of the photoelectric effect and Compton scattering. By adjusting the monoenergetic level, radiologists can tailor image properties to the diagnostic task. MIIs suffer less from scatter compared to conventional images, improving image contrast. Additionally, MIIs reconstructed at lower energy levels can accentuate attenuation differences, improving low-contrast resolution and thus the visibility of soft tissue and subtle tissue differences. Notably, the attenuation of iodinated contrast medium can be increased several times over. However, image noise can be amplified as well. Conversely, MIIs reconstructed at higher energy levels offer less soft tissue contrast but can assist in minimizing artifacts caused by dense materials.

Unlike material-specific images, which are primarily concerned with quantifying materials, MIIs allow for visualizing tissue structures across a spectrum of energies. This flexibility makes monoenergetic imaging a valuable diagnostic tool.

Polyenergetic images

The conventional image output from a non-DECT is the PI (Figure 3). The X-ray tube emits photons with a spectrum of energies, with the maximum energy determined by the set tube voltage. Photons which are not attenuated are captured and produce a signal in the detector. However, the low-energy photons will have a smaller impact on the signal produced in the detector than the high-energy photons. This down-weighting of low-energy photons, which are the primary carriers of contrast, has a degrading effect on image quality.

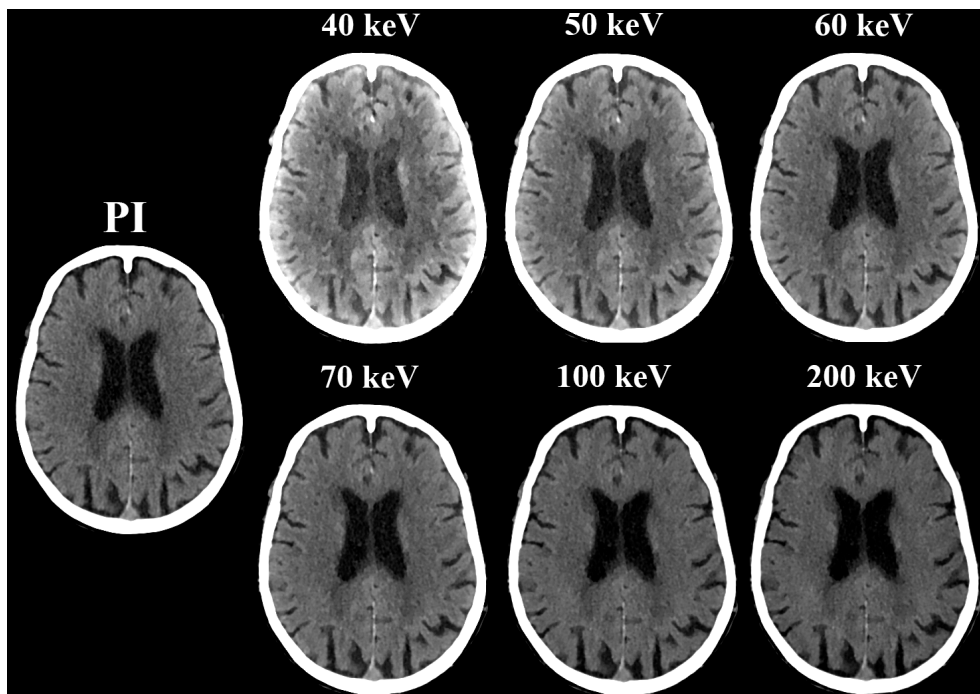


Figure 3.

Examples of polyenergetic (PI) and monoenergetic images at 40, 50, 60, 70, 100 and 200 keV, presented in the same window settings (C40/W80). The images are from one of the patients in **Paper II**, examined on a dual layer computed tomography (IQon Spectral CT, Philips Healthcare Inc., Best, The Netherlands).

Image quality

Noise

Image noise refers to the variation in HU and is quantified by standard deviation (SD) within a uniform region-of-interest (ROI). A high noise level has a negative effect on image quality, as it degrades anatomical visualization. Ideally, all pixels within the ROI would have the same HU value. However, quantum-, electronic- (system-specific) and reconstruction-related noise causes HU pixel values to vary around a mean. Quantum noise depends on the number of information carriers (photons). Thus, the noise level is directly related to the radiation dose, with increasing radiation dose reducing noise [11]:

$$SD \propto \frac{1}{\sqrt{n}} \quad (15)$$

where n is the number of photons. Consequently, the signal-to-noise ratio (SNR), defined as the signal intensity (HU) divided by the image noise (SD) improves in proportion to \sqrt{n} :

$$SNR = \frac{HU}{SD} \propto \sqrt{n} \quad (16)$$

Noise power spectrum (NPS) analysis provides a method for quantifying and characterizing image noise [11, 16]. NPS is typically measured in a region of an image where the signal is uniform and is computed by subtracting the mean pixel value from each pixel. This removes signal bias and ensures only the signal variation (noise) is analyzed. The signal variation is Fourier transformed decomposing it into spatial frequency components. Mathematically, NPS is expressed as:

$$NPS = \frac{\Delta n}{N} \sum |FT[HU - \overline{HU}]|^2 \quad (17)$$

where Δn is the pixel size, N the number of pixels, and \overline{HU} the mean value of the ROI. The resulting NPS curve illustrates the distribution of noise across spatial frequencies.

While SD and NPS analysis are useful for noise characterization, they must be applied and interpreted cautiously in patient images due to natural anatomical variations that can influence measurements.

Contrast resolution

Image contrast can be defined as the difference in attenuation values (HU) between two adjacent tissue types, or an object and its background. Low-contrast resolution, often referred to as soft tissue contrast or differentiation, is the ability to detect an object with similar attenuation as adjacent tissues or surrounding background.

High-contrast resolution is the ability to detect objects with distinct differences in HU relative to their surroundings. These objects can, for example, be small metal objects or calcifications and contrast-enhanced arteries. Unlike low-contrast resolution, high-contrast resolution is less sensitive to noise level. Instead, it is primarily limited by the difference in HU between object and surroundings and the spatial resolution of the image. The spatial resolution is determined by the physical size of the detector elements and the matrix size (i.e. how many pixels are used to create the image). Spatial resolution can be improved by reducing the reconstructed field of view, thereby maximizing the use of the available matrix size. Additionally, reconstruction filters can enhance both measured and perceived resolution by applying high-pass filtering and edge enhancement.

The contrast-to-noise ratio (CNR) provides a way to estimate image contrast while accounting for noise. CNR can be used to assess both low- and high-contrast resolution. It can be calculated in several different ways, with the simplest form being:

$$CNR = \frac{HU_{obj} - HU_{bkg}}{SD_{bkg}} \quad (18)$$

where HU_{obj} represents the mean attenuation value of an object, and HU_{bkg} and SD_{bkg} represents the attenuation and standard deviation, respectively, of the background [11]. Alternative formulations of CNR consider noise contributions from both the object and background [17-19].

$$CNR = \frac{HU_{obj} - HU_{bkg}}{\sqrt{SD_{obj}^2 + SD_{bkg}^2}} \quad (19)$$

or:

$$CNR = \frac{HU_{obj} - HU_{bkg}}{\sqrt{SD_{obj} + SD_{bkg}}} \quad (20)$$

Artifacts

Artifacts are objects or patterns in an image that do not correspond to real, physical structures. They can arise from technical malfunction or because of the chosen scan or reconstruction parameters. Additionally, they can be patient-related, such as motion during the scan or the presence of dense materials such as metal devices or prostheses.

Metal artifacts appear as alternating bright streaks and dark bands. They are predominantly caused by two phenomena: beam hardening and photon starvation. Beam hardening occurs when dense materials attenuate low-energy photons more effectively than high-energy photons, shifting the X-ray spectrum towards higher energies and thereby “hardening” it. This results in a misrepresentation of attenuation in the surrounding tissue, presenting as streak artifacts. Photon starvation occurs when nearly all photons are absorbed by a dense material, leading to insufficient signal in the detector and manifesting as streaks.

Scanning with low X-ray tube voltages results in more pronounced artifacts, since a low tube voltage means a larger proportion of low-energy photons, which are less likely to penetrate dense materials. Therefore, using a high tube voltage can aid in mitigating this artifact. In the same way, high-energy MIs can be used for artifact reduction.

Metal artifact reduction

To reduce metal artifacts, all CT scanner manufacturers have metal artifact reduction (MAR) algorithms [20-22]. Although the explicit details of the algorithms may be proprietary information, common methods involve iterative “sinogram inpainting” [23-26]. This process segments the metal regions in the image, creating a metal-only version, which is used to identify and remove projections with metal contribution from the sinogram. Projections with metal are replaced with interpolated values, modelling tissue in place of the metal. With each iteration, a correction image is generated and subtracted from the original, progressively refining the image. In the absence of metal, the algorithm should make no alterations to the image.

Artifact severity

The preferred method of assessing artifact severity is subjective analysis by human observers. However, observer studies are time-consuming and subject to potential bias, making objective and quantitative measures of artifact severity an appealing alternative.

A direct approach to assessing artifact severity or reduction involves surveying attenuation values to determine how closely HU values are restored to their true values. However, this requires prior knowledge of the true HU in the absence of artifacts.

Measuring the variation, in terms of SD, can also provide a simple estimation of artifact severity.

The artifact index is a straightforward method for quantifying artifact severity. It involves subtracting an “artifact-free” image from an image with artifacts, producing an “artifact-only” image. The absolute voxel values of the “artifact-only” image are then summed to provide a measure of artifact severity. However, because this method requires a reference image free from artifacts, it is not feasible for patient images.

Evaluation of streak artifacts using extreme value analysis

Streak artifacts, characterized by extreme high and low pixel values, can be statistically modelled and evaluated using extreme value analysis [27]. The largest difference between adjacent pixel values is estimated to be attributed to, and is considered a feature variable of, the artifacts.

Line profiles (i.e. measurements of HU along a line in the image) are placed perpendicular to the direction of the streaks to measure the difference in HU between adjacent pixels. The largest pixel differences, x , for the line profiles are arranged in ascending order: $x_1 \leq x_2 \leq \dots x_n$, where n is the number of line profiles. The Gumbel distribution, which has been used to evaluate streak artifacts and to model the distribution of the largest pixel differences, is expressed by [27-29]:

$$F(x) = \exp \left[-\exp \left(-\frac{x-\beta}{\gamma} \right) \right] \quad (21)$$

where $F(x)$ is the cumulative probability function for the largest pixel differences, x , and β and γ are location and scale parameters. $F(x)$ is unknown, but the estimated cumulative probability function, $\hat{F}(x_i)$, can be estimated using the mean rank method:

$$\hat{F}(x_i) = \frac{i}{n+1}, \text{ for } i = 1, \dots, n \quad (22)$$

The Gumbel plot is created by plotting the double logarithm of the estimated cumulative probability function against the largest pixel differences. By applying a linear fit ($ax + b$), the location and scale parameters can be estimated from the parameters a and b .

$$-\ln\{-\ln[\hat{F}(x)]\} = \frac{1}{\gamma}x - \frac{\beta}{\gamma} \quad (23)$$

From equation 23, the location parameter can be derived as $\beta = -b/a$, and used as an indicator of artifact severity.

Diagnostic performance

Receiver operating characteristics (ROC) curves are a key tool for objective evaluation of diagnostic performance. This method assesses not only image quality, but also the ability of the interpreting radiologist to make an accurate diagnosis based on observing the image. For ROC analysis to be possible, ground truth data is required, specifically knowledge of whether a patient has the condition being investigated [11, 30].

Performance metrics for ROC analysis are derived from a “truth table”, a 2x2 matrix categorizing diagnostic outcomes. This table includes the number of abnormal cases correctly identified as abnormal (true positive (TP)), abnormal cases incorrectly classified as normal (false negative (FN)), normal cases correctly classified as normal (true negative (TN)) and normal cases incorrectly classified as abnormal (false positive (FP)).

		<i>Truth</i>	
		Normal	Abnormal
<i>Observer response</i>	Normal	TN	FN
	Abnormal	FP	TP

The sensitivity (true positive fraction (TPF)) and specificity (true negative fraction (TNF)) are metrics used to evaluate the diagnostic performance of a test:

$$TPF = \text{Sensitivity} = \frac{TP}{TP+FN} \quad (24)$$

$$TNF = \text{Specificity} = \frac{TN}{TN+FP} \quad (25)$$

A test with high sensitivity will have a high chance of correctly identifying all cases with a condition, while a high specificity means that the test is good at ruling out the condition. The ROC curve is obtained by plotting the sensitivity as a function of false positive fraction (FPF) (Figure 4):

$$FPF = 1 - \text{Specificity} = \frac{FP}{TN+FP} \quad (26)$$

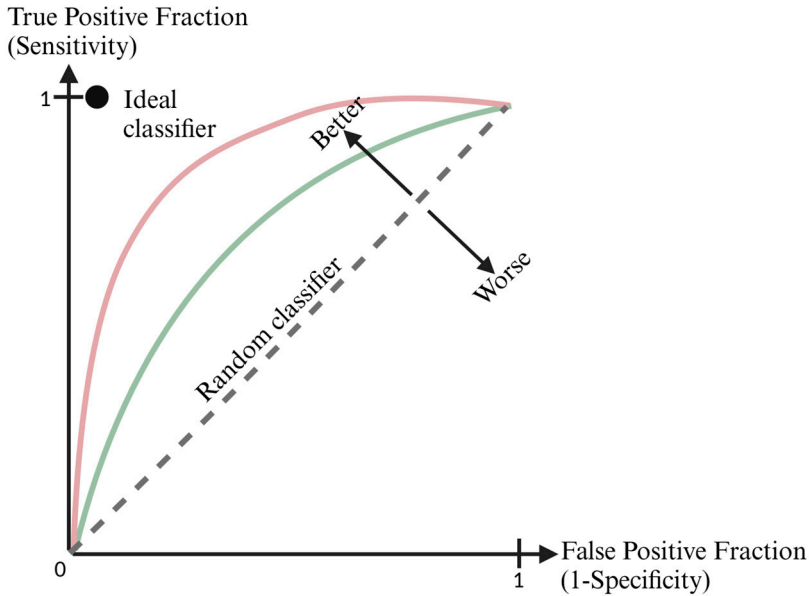


Figure 4.

Receiver operating characteristics (ROC) curves. The ideal classifier has a sensitivity and specificity of 1, generating an area-under-curve (AUC) of 1, while the random classifier has an AUC of 0.5. The pink ROC curve represents a diagnostic method with a better performance (larger AUC) than the green ROC. Created in BioRender. Fransson, V. (2025) <https://BioRender.com/jfdmud7>

The overall performance of a diagnostic method is commonly described by the area under the ROC curve. An ideal diagnostic method has an area under the curve (AUC) of 1 and delivers only correct diagnoses. Meanwhile, a method with an AUC of 0.5 is no better than flipping a coin. In practice, however, a high sensitivity comes at the cost of a lower specificity, and vice versa. Related metrics are the positive predictive value (PPV), the likelihood that someone who tests positive has the condition, and negative predictive value (NPV), the likelihood that someone who tests negative truly does not have the condition. The diagnostic accuracy is defined as the probability of making a correct diagnosis:

$$Accuracy = \frac{TP+TN}{TP+TN+FP+FN} \quad (27)$$

However, unlike the previous metrics, the accuracy is prevalence-dependent and should be interpreted with care.

Visual grading analysis

Visual grading analysis (VGA) is used to study the subjective aspects of image quality, in which observers (typically radiologists) are asked to review images regarding certain criteria [31-33]. Unlike ROC analysis, VGA does not require a known ground truth, allowing virtually any image to be used. Its moderate workload makes it feasible to include multiple observers, increasing statistical power [31, 32, 34]. However, its validity relies on the assumption that visibility of anatomical structures correlates with visibility of the pathology, which may not always hold true. VGA can be either absolute or relative, where absolute VGA means that images are reviewed individually, and relative VGA means that images are compared to each other.

VGA studies are susceptible to bias, including recognition bias, adaptation bias and observer selection bias [35-37]. Adaptation bias occurs if observers have developed a preference for a specific image appearance based on past experience, while recognition bias arises if radiologists recognize which image is acquired under which condition, effectively unblinding the study. Observers may either be experts in the field or more open to new imaging conditions than the average radiologist, potentially making the results less representative of routine clinical practice. VGA studies should include a sufficient number of cases and observers while minimizing the participation of observers involved in the study to reduce confirmation bias [37].

To facilitate diagnostic performance observer studies, including VGA or ROC, dedicated software, such as ViewDex (Viewer for Digital Evaluation of X-ray images), has been developed [38-40].

Absolute visual grading

In absolute VGA, observers evaluate individual images against criteria on an ordinal scale to estimate and compare image quality. Criteria can be based on established standards, such as the European Guidelines for quality criteria, or be customized for the study [34]. Grading scales typically include between four and five levels, from criterion not fulfilled (poor or non-diagnostic image quality) to criterion fulfilled (excellent image quality), with an even number of levels forcing a choice between poor or good quality and an odd number offering a middle “acceptable” level. Grading scales should be clinically relevant and tailored to the purpose of the study.

Relative and preference visual grading

In relative VGA, two or more images are reviewed simultaneously, with observers grading each image in comparison to a reference image. Grading scales can include between two (“worse” or “better”) and five levels (“much worse” to “much better”).

While intuitive and useful for capturing small differences, relative VGA has limited statistical possibilities, and all data rely on the quality of the reference image. A related method, the preference method, involves observers selecting their preferred image without using a reference image.

Visual grading characteristics analysis

Traditional statistical tests, such as the Mann Whitney U-test, fails to account for the complexity of VGA data, particularly the presence of multiple observers grading each case. This can lead to an underestimation of uncertainty and an increased risk of false positives, where the null hypothesis is incorrectly rejected. To address these limitations, a visual grading characteristics (VGC) analysis was developed [38, 41-44]. VGC is a non-parametric rank-invariant statistical method designed for VGA data. It enables the evaluation and comparison of image gradings obtained under two imaging conditions: a reference condition and a test condition. These conditions can differ in terms of scan protocols, CT systems, or reconstruction parameters, to name a few.

In VGC analysis, a VGC curve is generated – similar to the ROC curve of diagnostic performance (Figure 5). The x-axis presents the proportion of scores above a certain threshold for the reference condition, while the y-axis presents the same for the test condition. However, unlike ROC analysis, which compares the AUC value of two different diagnostic methods, VGC estimates the uncertainty in the area under one VGC curve (AUC_{VGC}). The AUC_{VGC} ranges between 0 and 1, values above 0.5 indicate that the test condition received higher grading scores, and values below 0.5 indicate that the reference condition received higher scores. The uncertainty in AUC_{VGC} is calculated using resampling techniques and presented with a 95% confidence interval.

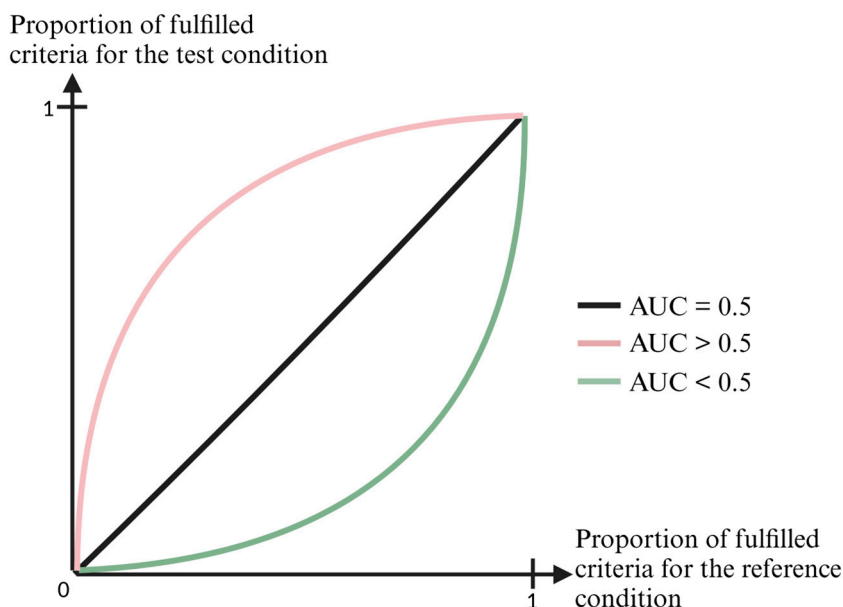


Figure 5.

Visual grading characteristics curves where the area-under-the-curve (AUC) is equal to 0.5 (reference condition and test condition had the same grading score), AUC higher than 0.5 (test condition received a higher score) and AUC lower than 0.5 (reference condition received a higher score). Created in BioRender. Fransson, V. (2025) <https://BioRender.com/9p1q3hk>

Inter- and intra-observer agreement

In a landmark tuberculosis study from 1947, researchers observed that experienced radiologists often disagreed when interpreting radiographic images. Moreover, the same radiologist could assess the same image differently at different times [45]. This inconsistency introduces uncertainty in observer studies and remains a challenge today. However, this inconsistency can be minimized by including a large, representative number of observers, ensuring the task is well-defined and understood, and providing all observers with the same information.

In the context of VGA, inter-observer agreement refers to the consistency among different observers, while intra-observer agreement is the reliability of a single observer across multiple sessions. Observer agreement can be measured using the weighted Cohen's kappa coefficient [46]. Kappa values range from -1 (perfect disagreement) to +1 (perfect agreement), with 0 representing chance agreement. Altman's interpretation categorizes kappa values as follows [47]:

<0 = poor
0.01–0.20 = slight
0.21–0.40 = fair
0.41–0.60 = moderate
0.61–0.80 = substantial
0.81–1.00 = almost perfect

Cohen's kappa was developed to control for random agreement, assuming observer independence, which can sometimes excessively lower the calculated agreement [48]. It is sensitive to the grading scale and the distribution of scores [16]. For example, when agreement is high, but the grading scale has few options, kappa may yield unexpectedly low values due to the high potential of a chance agreement.

An alternative measure is percent agreement, which is calculated as the proportion of instances observers are in total agreement. While this method does not account for chance agreement and may overestimate reliability, it is useful when random guessing is unlikely [48].

Neuroradiology

Stroke imaging

Stroke is the sudden loss of neurological function due to a reduced or interrupted blood flow, and consequently oxygen supply, to brain cells. Stroke can be ischemic, caused by an occlusion (blocked artery), or hemorrhagic, caused by a ruptured artery (Figure 6). Symptoms vary depending on the affected brain region but without intervention the lack of oxygen will cause rapid cell death. The common saying “Time is brain” emphasizes the need for swift treatment [49, 50].

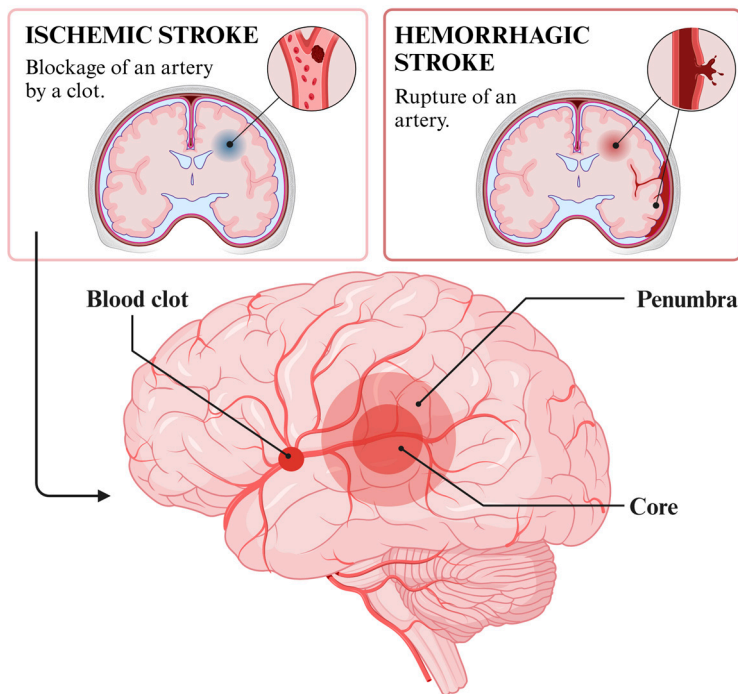


Figure 6.

Illustrations of an ischemic and hemorrhagic stroke, with resulting penumbra and core region. Created in BioRender. Fransson, V. (2025) <https://BioRender.com/ppozoda>

CT is the most common imaging modality for diagnosing acute stroke [51]. While positron emission tomography (PET) is the gold standard for perfusion imaging, it is time-consuming and often impractical. Diffusion magnetic resonance imaging (MRI) is highly sensitive to ischemic changes but is less accessible than CT, which offers rapid

imaging with high sensitivity for hemorrhage and the ability to detect occlusions [52]. For moderate to severe ischemic stroke, the ability of CT to detect ischemic damage has been found to be comparable to diffusion MRI [53]. However, early ischemic changes – characterized by loss of gray and white matter differentiation – and small lesions remain challenging to detect [50, 54, 55].

Stroke imaging with CT

Non-contrast CT (NCCT) is a brain CT scan without contrast enhancement. It is the first choice of imaging in stroke diagnosis and used for soft tissue assessment, offering a high sensitivity for hemorrhage and the ability to visualize ischemic lesions depending on the extent of the damage (Figure 7).

CT perfusion (CTP) is performed to evaluate blood flow and blood volume in brain tissue, indirectly indicating the oxygenation status of the tissue (Figure 7). It involves injecting the patient with CM, then performing a dynamic imaging sequence to monitor the passage of the CM through the brain. Specialized software analyzes the CT images to estimate perfusion parameters such as cerebral blood volume (CBV), cerebral blood flow (CBF) and mean transit time (MTT) for the CM passage [56]. These parameters are used to define penumbra (potentially salvageable tissue) and core (irreversibly damaged tissue). The volumetric mismatch between penumbra and core aids in identifying patients who may benefit from recanalization treatment (interventions to reopen an occluded artery, intravenous thrombolysis or endovascular thrombectomy). By providing additional information on tissue condition, CTP improves treatment decisions beyond merely using time thresholds [57].

CT angiography (CTA) is performed for arterial visualization and to identify occlusions, timed to coincide with the CM's peak-arterial phase. In recent years, multiphase CTA (mCTA) has become a common examination (Figure 7) [58-60]. mCTA involves three scans: the first during the peak-arterial phase of the CM, the second during the peak-venous phase and the third during the late-venous phase. This technique indirectly assesses perfusion by evaluating the collateral blood flow.

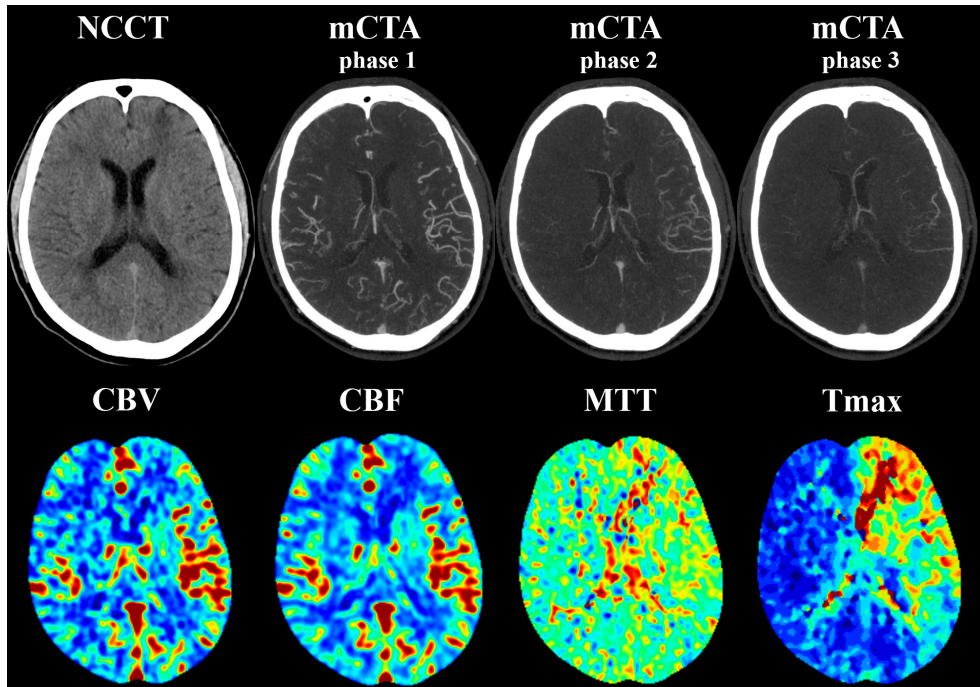


Figure 7.

Images from one of the patients in **Paper I**, examined on a dual layer computed tomography (CT) scanner (iQon Spectral CT, Philips Healthcare Inc., Best, The Netherlands) and perfusion data analyzed by Rapid (RapidAI, Menlo Park, CA, USA). **Top)** Non-contrast CT (NCCT) followed by the three phases of multiphase CT angiography (mCTA). The first phase corresponds to a conventional CT angiography. **Bottom)** CT perfusion maps: CBV – Cerebral blood volume, CBF – Cerebral Blood Flow, MTT – Mean Transit Time, Tmax – Time to maximum contrast enhancement.

Artifacts in brain imaging

Brain imaging is challenged by the presence of dense, highly attenuating materials, such as bone and occasionally metal, coils or stents from previous interventions. These high-attenuating materials cause streak artifacts which degrades image quality and may obscure pathologies. Filtration and correction algorithms are implemented to compensate for beam hardening effects originating from the skull. But in the posterior fossa region, artifacts typically remain post-correction.

For metal objects, MAR algorithms are commonly used. MIs have been suggested for further artifact reduction, and the combination of MAR and high-energy MI has been shown to have an additive effect in reducing artifacts.

Differentiation of gray and white matter

Differentiation between gray and white matter is necessary for accurate diagnosis of early ischemia, ischemic lesions and other brain pathologies. This differentiation is improved by achieving a higher low-contrast resolution.

CT imaging is typically performed with X-ray tube voltages ranging from 70 to 150 kV. This produces an X-ray spectrum consisting of a wide range of photon energies, with a maximum energy corresponding to the tube voltage, and a much lower mean energy. At low photon energies, the photoelectric effect, which is highly dependent on atomic number, plays a dominant role in determining image contrast. However, in conventional single- and dual-energy CT systems with energy-integrating scintillator detectors, high-energy photons contribute more heavily to the signal, effectively downweighing the low-energy photons and degrading soft tissue contrast. Spectral CT provides a potential solution to this problem with the generation of MIs, especially MIs reconstructed at low energies since the visible and measurable attenuation difference between gray and white matter increases at lower energies (Figure 3, Figure 8).

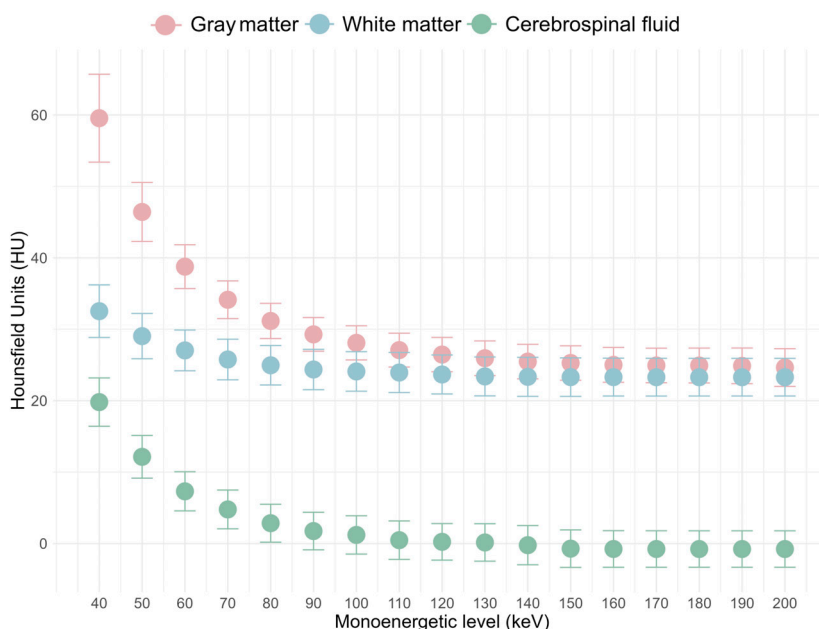


Figure 8.

Example of how the attenuation, represented by Hounsfield units (HU), of gray matter, white matter and cerebrospinal fluid can vary as a function of monoenergetic level (keV). Created using data from a patient in **Paper II**, examined on a dual layer computed tomography (IQon Spectral CT, Philips Healthcare Inc., Best, The Netherlands).

Contrast medium

Iodinated CM plays a key role in CT brain imaging by enhancing the visibility of vascular structures and improving the differentiation between normal and pathological tissue. Despite its diagnostic benefits, the use of CM carries potential risks in the form of contrast-induced nephropathy (CIN) [61-64]. CIN is a serious complication which may result in acute kidney injury and is associated with myocardial infarction and neurological complications. The risk of CIN varies between patients, with the most important risk factors being a pre-existing renal disease and diabetes [62, 64, 65]. Administering higher CM doses is associated with a higher risk of CIN. Preventive measures, such as ample hydration and minimizing the CM dose, are commonly used for high-risk patients.

Since iodine's K-edge is at 33 keV, scanning with low tube voltages can increase CM attenuation, enabling lower doses of CM [66-69]. The visualization of contrast-enhanced vascular structures is less sensitive to image degradation from increased noise, compared to soft tissue, making it more feasible to perform examinations with low tube voltage. Low-energy MI reconstructions from spectral CT are also a viable alternative as the CM attenuation increases at lower energies (Figure 9).

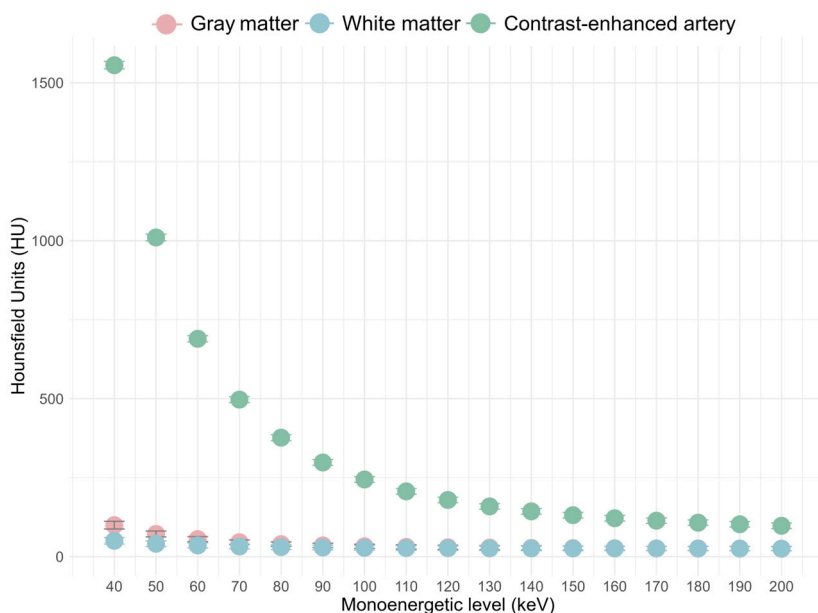


Figure 9.

Example of how the attenuation, represented by Hounsfield units (HU), of gray matter, white matter and an contrast-enhanced artery can vary as a function of monoenergetic level (keV). Created using data from a patient in **Paper III**, examined on a dual layer computed tomography (IQon Spectral CT, Philips Healthcare Inc., Best, The Netherlands).

Radiation dose and associated risks

When optimizing diagnostic images, the radiation dose from X-ray exposure should follow the concept of ALARA. The radiation dose should be just high enough for the image quality to be good enough for the diagnostic task. Reducing the dose too much can result in a non-diagnostic image quality, and consequently misdiagnosis or need for additional imaging – ironically increasing the total radiation dose delivered. All X-ray examinations must always be medically motivated. In a critical situation, for example when there is suspicion of stroke, the number one priority is a swift examination and diagnosis – followed by a timely and correct treatment of the condition – which means that a relatively high radiation dose may be necessary to improve patient outcome.

Ionizing radiation is harmful due to its ability to damage the deoxyribonucleic acid (DNA), causing DNA strand breakage and leading to cell death, mutation or carcinogenesis. Radiation effects, describing the potential biological consequences of the radiation, are divided into stochastic (probabilistic) and deterministic (radiation-level based) effects. Deterministic effects will arise when the radiation dose exceeds a certain threshold, becoming more severe as the dose increases. Stochastic effects are primarily radiation-induced cancer. Although debated, the most established model for risk assessment is the linear-no-threshold (LNT) model, stating there is no lower threshold for radiation effects [70-72]. Rather, all radiation is considered harmful, and the risk of stochastic effects increases with dose.

The effective dose concept was developed to estimate the risk associated with exposure to radiation and should be used on a population level, rather than for individuals. Effective dose, E , is defined as [73, 74]:

$$E = \sum_T w_T \cdot \sum_R w_R \cdot D_{T,R} \quad (28)$$

where $D_{T,R}$ is the absorbed dose. It considers the radiation type (w_R) and varying radiosensitivity, of human organs and tissue using a tissue weighting factor (w_T). Given that the radiation weighting factor, w_R , for photon exposure is 1, the equation becomes:

$$E = \sum_T w_T \cdot D_T \quad (29)$$

Radiation dose in CT imaging

Modern hardware, for example dynamic collimators, and software solutions, such as iterative or deep learning-based reconstruction, have in recent years enabled high quality CT imaging using lower radiation doses than was previously possible. Three-dimensional automatic exposure control has enabled radiation doses adjusted to patient size and diagnostic task. Despite these advancements, the radiation dose associated with CT examinations remains relatively high. The number of examinations per capita has increased over time, resulting in an increased collective effective dose [75-77]. To monitor radiation dose from medical CT examinations, a solid model for dose estimation is required.

The radiation dose in CT imaging is measured using the CT dose index (CTDI) by volume ($CTDI_{vol}$). When CTDI first came into use, scans were acquired using single-slice axial scanning. The International Electrotechnical Commission defined $CTDI_{100}$ as the absorbed dose for one axial scan of 100 mm [78]. $CTDI_{100}$ is measured using an ionization chamber with an active length of 100 mm, either in air or in a 15 cm long cylindrical polymethyl methacrylate (PMMA) phantom of 16 cm diameter, representing a head, or 32 cm, representing a body. Since the in-plane distribution of absorbed dose varies, a weighted CTDI ($CTDI_w$) was introduced, where $CTDI_{100}$ was measured both centrally and peripherally:

$$CTDI_w = \frac{1}{3}CTDI_{100,central} + \frac{2}{3}CTDI_{100,peripheral} \quad (30)$$

To account for axial scan spacing, or helical scanning, CTDI by volume ($CTDI_{vol}$) was introduced:

$$CTDI_{vol} = \frac{CTDI_w}{pitch} \quad (31)$$

where pitch is the table movement per rotation, relative to the collimated beam width. The $CTDI_{vol}$ value is displayed at the console before scanning and is available after the scan. It represents the output from the scanner and will only depend on the scan parameters – not the patient size, shape or body composition [79-81]. As such, it does not represent the true absorbed dose to the patient.

As examinations vary in scan length, dose length product (DLP) was introduced to provide a representation of the total absorbed dose:

$$DLP = CTDI_{vol} \cdot L \quad (32)$$

where L is the scan length. DLP can be translated to effective dose, E , using an anatomy-specific conversion factor, k :

$$E = DLP \cdot k \quad (33)$$

The size specific dose estimate (SSDE) is an alternative to $CTDI_{vol}$ which is becoming more common on modern CT scanners. SSDE takes patient size into account by multiplying the $CTDI_{vol}$ with a size-specific conversion factor. The conversion factor is determined by the patient's size and/or tissue composition and is derived from the scout images.

In Table 1, average radiation doses ($CTDI_{vol}$, DLP and effective dose) are listed for the neuroradiological examinations studied in this thesis. The data are based on the average doses from CT systems at Skåne University Hospital in Lund in 2023. Effective dose was calculated using conversion factors based on weighting factors defined by the International Commission on Radiological Protection (ICRP), 0.0024 mSv/(mGy·cm) for brain (16 cm CTDI-phantom) and 0.009 mSv/(mGy·cm) for combined brain and neck imaging (32 cm CTDI-phantom) [82].

Table 1.

Radiation dose (average \pm standard deviation) for all examinations, performed at any computed tomography (CT) scanner, at Skåne University Hospital in Lund in 2023. Effective dose is calculated using conversion factors based on tissue weighting factors from the ICRP Publication 103 [82].

	Non-contrast brain CT <i>16 cm CTDI-phantom</i>	CT angiography of the neck and brain <i>32 cm CTDI-phantom</i>	Brain CT perfusion <i>16 cm CTDI- phantom</i>
$CTDI_{vol}$ [mGy]	42.3 (± 6.4)	12.5 (± 7.8)	67.5 (± 16.8)
DLP [mGy·cm]	855 (± 164)	502 (± 168)	540 (± 155)
Effective dose [mSv]	2.1 (± 0.4)	4.5 (± 1.5)	1.3 (± 0.4)

$CTDI_{vol}$ – volumetric computed tomography dose index, DLP – dose length product.

Summary of the studies

This section summarizes the methodologies used for **Papers I-IV**, including study design, inclusion criteria, patient characteristics and CT scan parameters. Detailed descriptions of materials and methods can be found in their respective papers.

Data collection

The data in this thesis were obtained from CT images of 190 participants in total, distributed across four studies (Table 2). All participants were patients who underwent CT examinations in the below-listed CT systems at Skåne University Hospital in Lund between 2018 and 2023. Patients were retrospectively included from the hospital's picture, archiving and communication system based on the inclusion criteria defined for each study. To minimize systematic errors and selection bias, examination codes and filters were applied to include consecutive examinations that met the criteria. Access to spectral data files was a criterion for inclusion, as they are required for retrospective generation of MIs and ID maps.

Table 2.

Summary of the total number of participants, examination type, CT systems and reconstructions for each paper, and whether analysis of phantom images were performed or not.

	Paper I	Paper II	Paper III	Paper IV
Total number of participants	10	52	127	1
Examination type	NCCT, CTP, mCTA	NCCT	CTA	NCCT
CT system(s)	IQon Spectral CT ^a	IQon Spectral CT ^a	IQon Spectral CT ^a	IQon Spectral CT ^a , Naeotom Alpha ^b
Reconstruction	PI, ID, MI at 40 keV	PI, MI at 40-200 keV	PI, MI at 40-200 keV	PI, MI at 40-190 keV
Phantom analysis	No	No	No	Yes

CT – computed tomography, CTA – CT angiography, CTP – CT perfusion, ID – iodine density, mCTA – multiphase CTA, MI – monoenergetic image, NCCT – non-contrast CT, PI – polyenergetic image.

^a Philips Healthcare Inc., Best, The Netherlands, ^b Siemens Healthineers, Forchheim, Germany

Ethical considerations

All examinations included in the studies were clinically indicated and performed as part of standard clinical practice. Consequently, patients were not subject to additional examinations or radiation exposure. There were no risks or benefits associated with inclusion in the studies. Informed consent was waived, as all studies were retrospective in nature and involved no intervention, thus minimizing participation bias. Ethical approval for all studies was obtained from the Swedish Ethical Review Authority (reference no. 2019-02225) and informed consent was waived by the authority.

Statistical methods

Statistical methods were employed to analyze and compare results, providing estimates of whether observed differences were statistically significant. Parametric tests were used for data considered normally distributed, while non-parametric tests were applied when distributions could not be confidently classified as normal. The confidence level for all statistical tests was set at 95%, with a p-value threshold of 0.05 used to determine statistical significance.

The statistical tests used in this thesis were predominantly non-parametric. For paired continuous and ordinal data, the Wilcoxon signed rank test was applied (**Papers II-III**). For nominal data, the Chi-square test was utilized (**Papers II-III**). In the case of continuous data with independent observations, the Mann-Whitney U-test was utilized (**Papers II-III**). VGC data were evaluated using VGC analysis (**Paper III**).

Paper I

We aimed to investigate whether mCTA can be used to distinguish underperfused from normal tissue, similar to CTP. mCTA is less technically demanding than CTP and has the added benefit of whole brain coverage and arterial visualization. We based our method on the hypothesis that iodine attenuation in two corresponding regions in the left and right hemisphere should only display major differences when there is a perfusion deficit present in either one of them. Additionally, we wanted to determine if this difference was enhanced using low-energy MIs or ID, compared to PIs.

Patients were eligible for inclusion if they had performed a NCCT, mCTA and CTP examination due to suspicion of stroke. Ten patients were identified who fit the criteria,

five with perfusion deficits and five with normal perfusion. Scan and reconstruction parameters are listed in Table 3, while patient characteristics are presented in Table 4.

Table 3.

Scan and reconstruction parameters.

Parameters	NCCT	CTP	mCTA
Tube voltage [kV]	120	80	120
Tube loading for average adult, mAs	220 (DRI 35)	75	162 (DRI 24)
Collimation [mm]	64x0.625	64x0.635	64x0.625
Pitch	0.359	1.000	1.015
Rotation time [s]	0.33	0.5	0.5
Contrast medium [ml]	NA	40	60
Reconstruction method and kernel	iDose level 1, UB	iDose level 5, UA	iDose level 3, C
Slice thickness [mm]	10	5	10
Reconstructions	PI, ID, MI at 40 keV	PI	PI, ID, MI at 40 keV

CT – computed tomography, CTA – CT angiography, CTP – CT perfusion, ID – iodine density, mCTA – multiphase CTA, MI – monoenergetic image, NCCT – non-contrast CT, PI – polyenergetic image, NA – not applicable.

Table 4.

Patient characteristics and radiation dose exposure.

Patient characteristics	Patients with perfusion deficits (n=5)			Patients with normal perfusion (n=5)		
Age (IQR) [years]	62 (5)			73 (15)		
Sex: F/M (%/%)	1/4 (20%/80%)			3/5 (60%/40%)		
Radiation dose	NCCT (16 cm)	CTP (16 cm)	mCTA (32 cm)	NCCT (16 cm)	CTP (16 cm)	mCTA (32 cm)
CTDI _{vol} (IQR) [mGy]	41.3 (3.2)	4.5	15.1 (6.5)	44.7 (1.8)	4.5	13.5 (5.4)
DLP (IQR) [mGy·cm]	893 (52)	540	1063 (339)	893 (63)	540	991 (317)
Effective dose (IQR) [mSv]	2.1 (0.1)	1.3	5.1 (1.7)	2.1 (0.1)	1.3	4.9 (1.6)

CT – computed tomography, CTA – CT angiography, CTP – CT perfusion, CTDI_{vol} – volumetric computed tomography dose index, DLP – dose length product, F – female, IQR – interquartile range, M – male, mCTA – multiphase CTA, NCCT – non-contrast CT.

For the mCTA examination, three spiral scans were acquired eight seconds apart after CM injection, to capture the CM in three different phases: peak-arterial phase, venous phase and late-venous phase. In the CTP examination, sequenced scans were acquired every four seconds for sixty seconds total, to capture the entirety of the CM passage.

Regions with perfusion deficits were identified from the CTP results (penumbra and core). PIs, MIs at 40 keV and ID maps were constructed and analyzed for the NCCT

and mCTA scans. HU in PIs and MIs, and iodine concentration in ID maps, were measured in 11 ROIs across six axial planes corresponding to the major arterial territories of the brain, using the Alberta Stroke Programme Early CT Score method (Figure 10) [83].

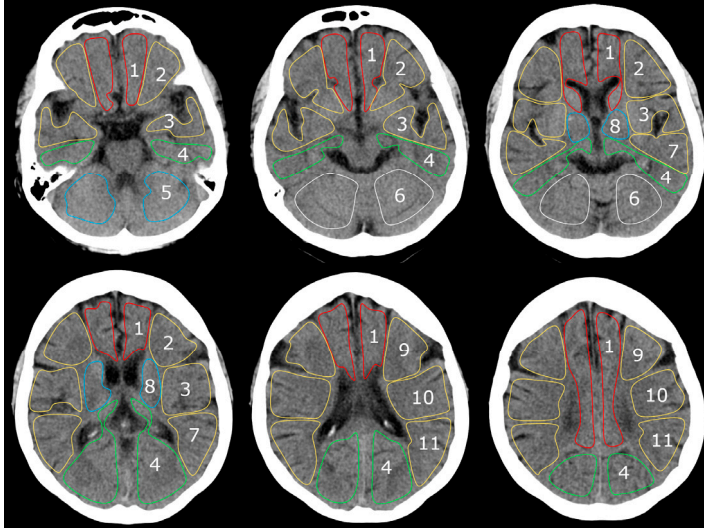


Figure 10.

Region-of-interest placement for the quantitative measurements. The numbers corresponds to arterial territories: (1) anterior cerebral artery, (2) middle cerebral artery (M) subartery M1, (3) M2, (4) posterior cerebral artery, (5) posterior inferior cerebral artery, (6) superior cerebellar artery, (7) M3, (8) lenticulostriate arteries, (9-11) M4-M6. Adopted from **Paper I**.

To quantify the difference in attenuation between regions in the left and right hemisphere, we developed a measure called “maximum value of derivative” (MVD). For each arterial territory, data points were normalized by their baseline value from the NCCT scan. For each phase, the ratio between corresponding ROIs in the right and left hemisphere was calculated and derived with respect to time, resulting in plots communicating how rapidly the ratio changed. MVD, the maximum change in ratio, was used to assess the magnitude of underperfusion. An MVD of zero would mean normal perfusion. A positive MVD would be indicative of a perfusion deficit in the right hemisphere, as the right side would experience a delayed or absent contrast enhancement. In the same way, a negative MVD would be indicative of a perfusion deficit in the left hemisphere. A step-by-step development of MVD can be seen in Figure 11, and the mathematical definition of MVD was:

$$MVD = \max \frac{\partial}{\partial t} \left(\frac{(HU \text{ or } ID)_{right}}{(HU \text{ or } ID)_{left}} \right) \quad (34)$$

A reliable method for detection of perfusion deficits should produce MVDs for regions with perfusion deficits, which are high enough to distinguish from the MVDs of regions with normal perfusion. The change in HU or iodine concentration and the MVD were quantitatively compared between the three reconstructions (PIs, MIs at 40 keV and ID) regarding how well they were able to separate normal from underperfused regions.

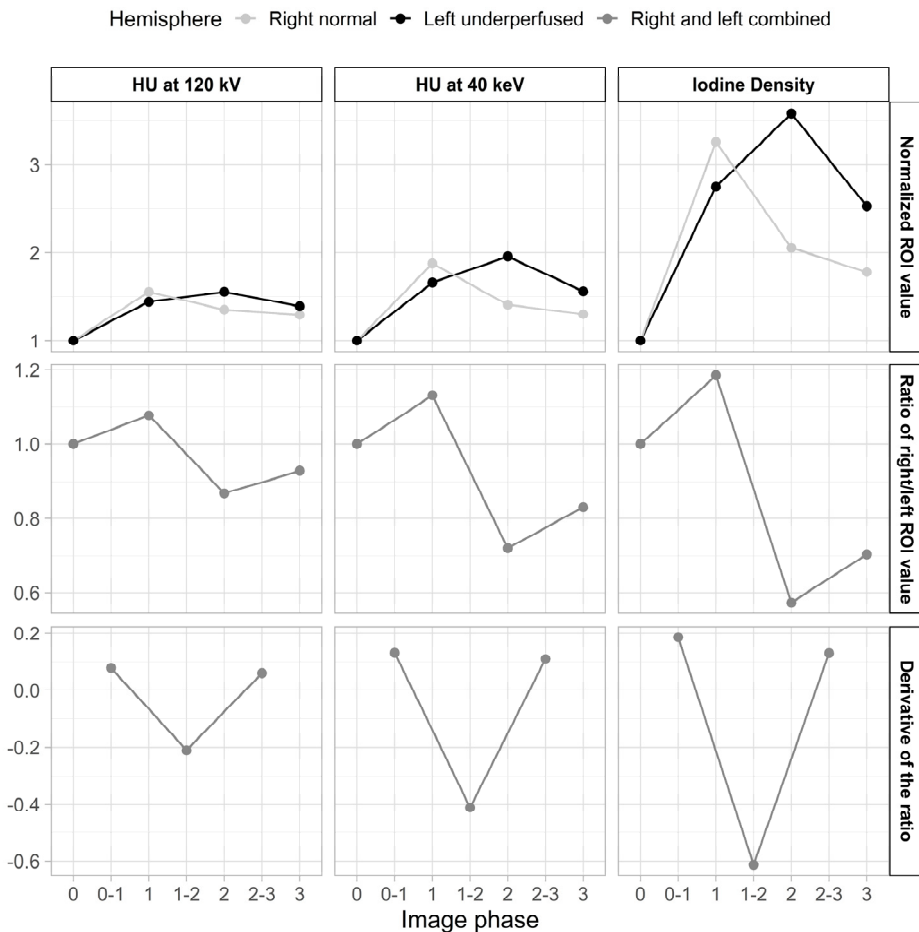


Figure 11.

Top row: Hounsfield units (HU) and iodine density (ID) measured in regions-of-interest (ROI) and normalized to the ROIs baseline (phase 0) value in right (normal) and left (underperfused) hemispheres across four image phases. Phase 0 represents the non-contrast computed tomography (CT), and phases 1–3 correspond to the three phases of the multiphase CT angiography. “0-1” indicates the transition between phase 0 and 1. **Middle row:** Ratio of HU and ID in the right and left hemisphere. **Bottom row:** The derivative (i.e. change) of the ratio between consecutive image phases. In this example, the maximum derivative of the ratio (MVD) was found between phases 1 and 2. Adopted from **Paper I**.

Paper II

In this study, we evaluated the image quality and diagnostic ability of PIs and MIs to detect acute ischemic stroke, using quantitative and qualitative methods.

Patients who underwent a NCCT scan, and had a confirmed acute, cortical ischemic lesion on either the initial CT or follow-up examination, were included. The negative control group consisted of patients who underwent NCCT but did not have any acute ischemic lesions or other pathologies. Patient characteristics and imaging parameters are listed in Table 5.

Table 5.

Patient characteristics, radiation dose, scan and reconstruction parameters.

Patient characteristics and radiation dose	Patients with ischemic lesions (n=29)	Patients without ischemic lesions (n=23)
Median age (IQR) [years]	67 (19)	63 (39)
Sex: F/M (%/%)	9/20 (31%/69%)	11/12 (48%/52%)
Median maximum diameter of ischemic lesion (IQR) [cm]	3 (2.9)	NA
Median CTDI _{vol} (16 cm) (IQR) [mGy]	40.1 (5.6)	36.5 (5.1)
Median DLP (16 cm) (IQR) [mGy·cm]	826 (98)	751 (149)
Median effective dose (IQR) [mSv]	2.0 (0.3)	1.7 (0.4)
Scan and reconstruction parameters		
Tube voltage [kV]	120	
Automatic dose modulation	DRI 37	
Collimation [mm]	64x0.625	
Pitch	0.36	
Rotation time [s]	0.33	
Reconstruction method and kernel	iDose level 1, UB	
Slice thickness [mm]	3	
Reconstructions in quantitative analysis	PI, MI at 40-200 keV	
Reconstructions in qualitative analysis	PI, MI at 50, 60 and 70 keV	

CTDI_{vol} – volumetric computed tomography dose index, DLP – dose length product, DRI – dose right index, F – female, IQR – interquartile range, M – male, MI – monoenergetic image, NA – not applicable, PI – polyenergetic image.

For the quantitative analysis, HU and SD were measured for ischemic gray matter, normal gray matter and normal white matter (Figure 12). The ischemic gray matter ROI was placed using follow-up imaging as a guide. Difference in attenuation and

CNR was calculated between gray matter (ischemic and normal) and white matter, as well as between ischemic and normal gray matter, and compared across reconstructions.

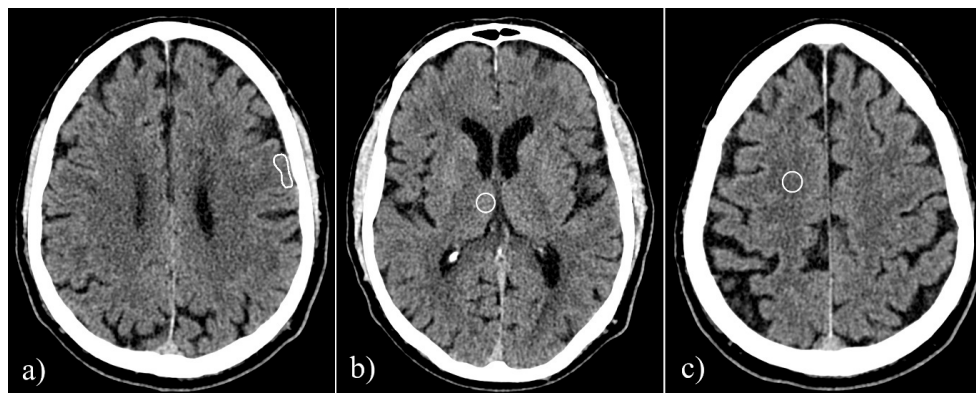


Figure 12.

a) Ischemic gray matter, b) normal gray matter , and c) normal white matter. Adopted from **Paper II**.

Qualitative image quality of PIs and MIs at 50, 60 and 70 keV were analyzed using absolute and relative VGA. The absolute VGA included patients with confirmed ischemic lesions, with two observers asked to grade the images using a five-point grading scale (1 – Non-diagnostic, 2 – Poor, 3 – Fair, 4 – Good, 5 – Excellent) for:

1. Overall impression of image quality
2. Impression of image ability of diagnosing acute ischemia

The relative VGA was performed in supervised viewing sessions and included patients both with and without ischemic lesions. For each patient, two observers had access to both PI and MIs at the same time and were asked to identify:

1. The presence of an ischemic lesion (yes/no)
2. If yes, infarct location
3. Which reconstruction was best to visualize ischemic lesions

Follow-up CT or MRI was used to determine whether the observers were correct in their identification and localization of ischemia. Diagnostic performance was determined and compared between the original clinical report (by the attending radiologist in the acute stage, with access to PIs only) and the VGA study (observers with access to both PIs and MIs at 50, 60 and 70 keV).

Paper III

In this study, we evaluated whether MIs reconstructed from CTA could increase arterial visualization and compensate for reduced contrast enhancement due to reductions in CM dose or poorly timed examinations. Our hypothesis was that low-energy MIs could return image quality to that of PIs with full contrast timing or optimal timing.

Patient characteristics and imaging parameters are listed in Table 6. Patients were excluded if they had an internal carotid artery (ICA) or middle cerebral artery (MCA) occlusion. Participants were randomly assigned to a protocol group based on their exam date and each protocol was performed for a limited period.

Table 6.

Patient characteristics, radiation dose, scan and reconstruction parameters.

Patient characteristics and radiation dose	Group 1. Full CM dose (n=52)	Group 2. Half CM dose (n=24)	Group 3. Half CM dose, optimized timing (n=39)
Median age (IQR) [years]	68 (18)	75 (26)	72 (22)
Sex: F/M (%/%)	22/30 (42%/58%)	11/13 (45%/54%)	23/16 (59%/41%)
Median CTDI _{vol} (32 cm) (IQR) [mGy]	12.3 (4.6)	12.2 (4.2)	14.6 (6.5)
Median DLP (16 cm) (IQR) [mGy·cm]	509 (240)	511 (198)	586 (249)
Median effective dose (IQR) [mSv]	2.5 (1.2)	2.5 (1.0)	2.7 (1.2)
Scan and reconstruction parameters			
Tube voltage [kV]	120		
Automatic dose modulation	DRI 24		
Collimation [mm]	64x0.625		
Pitch	0.609	0.609	0.797
Rotation time [s]	0.50	0.50	0.33
Intravenous contrast medium [ml]	60	30	30
Reconstruction method and kernel	iDose level 3, B		
Slice thickness [mm]	2		
Reconstructions in quantitative analysis	PI, MI at 40-200 keV		
Reconstructions in qualitative analysis	PI, MI at 50-60 keV		

CM – contrast medium, CTDI_{vol} – volumetric computed tomography dose index, DLP – dose length product, DRI – dose right index, F – female, IQR – interquartile range, M – male, MI – monoenergetic image PI – polyenergetic image

Quantitative and qualitative measures of image quality were compared between Groups 1 and 3 to determine if MIs with 50% reduction in CM dose (Group 3) were of equal image quality as PIs with full CM dose (Group 1). MIs with poor contrast timing (Group 2) were compared to PIs with optimized timing (Group 3) to determine if MIs could enhance arterial visualization and compensate for the suboptimal timing.

Quantitatively, the arterial attenuation (HU), SNR and CNR in two arteries (ICA and M2 segment of the MCA) were analyzed. Homogenous white matter was used as the background tissue for CNR calculations.

To assess the contrast timing, venous attenuation in the confluence of sinuses was measured (in the PI only) and used to calculate a vein-to-artery ratio ($HU_{\text{vein}}/HU_{\text{ICA}}$). All ROIs were sized to include as much tissue as possible without risking partial volume effects.

For qualitative image quality assessment, absolute VGA was performed, and the result was analyzed using VGC analysis. Five observers were asked to assess the PI and MI at 50 keV and 60 keV regarding four criteria:

1. Overall image quality
2. Visual representation of the internal carotid artery
3. Visual representation of the M2 segment of the middle cerebral artery
4. Timing of the examination

Criteria 1-3 were graded using a five-point scale (1 – Non-diagnostic, 2 – Poor, 3 – Fair, 4 – Good, 5 – Excellent) and for criterion 4 the observers could select between early arterial, late arterial or venous phase.

Paper IV

In a previous study by our research group, quality of images reconstructed from brain CTs with intracranial coils, without using MAR, was studied [22]. The results indicated that MIs improved soft tissue differentiation and did not increase artifact severity, compared to PIs. However, we found it challenging to perform objective, quantitative measurements of artifact severity in patient images. In this study, we aimed to facilitate artifact quantification using an anthropomorphic brain phantom. At the time of data collection for the previous study, MAR was not part of the clinical routine. Thus, we investigated how the combination of MI and MAR affects both visualization of soft tissue and artifact severity.

Scans from one patient were included. The patient had undergone coil treatment due to a subarachnoid hemorrhage and was scheduled for multiple follow-up examinations. The brain phantom had a cylindrical cavity, enabling scans both with and without coils. Scan and reconstruction parameters are listed in Table 7.

Table 7.

Scan and reconstruction parameters for the studied examinations.

	Dual layer CT	Photon counting CT
Tube voltage [kV]	120	
Effective tube loading [mAs]	305	228
Collimation [mm]	64x0.625	48x0.4
Pitch	0.36	0.35
Rotation time [s]	0.33	0.5
Median CTDI_{vol} (16 cm) (IQR) [mGy]	52.5	45
Reconstruction method and kernel	iDose level 1, UB	QIR level 4, Hr36
Type of MAR	O-MAR	iMAR, Neuro Coils
Slice thickness [mm]	1	
Reconstructions in quantitative analysis	PI, MI at 40-190 keV with and without MAR	
Reconstructions in qualitative analysis	PI, MI at 60, 80, 100, 120 and 140 keV with and without MAR	

CT – computed tomography, CTDI_{vol} – volumetric computed tomography dose index, IQR – interquartile range, MAR – metal artifact reduction, MI – monoenergetic image, PI – polyenergetic image.

Quantitative analysis was performed using the phantom images. HU, SD and artifact index (the summative difference between an image with and without metal) were measured in a U-shaped ROI (Figure 13). Gumbel distribution analysis was performed to estimate the location parameter as an indicator of artifact severity. A low artifact severity was defined as HU close to that of the ground truth, low values of SD, artifact index and location parameter.

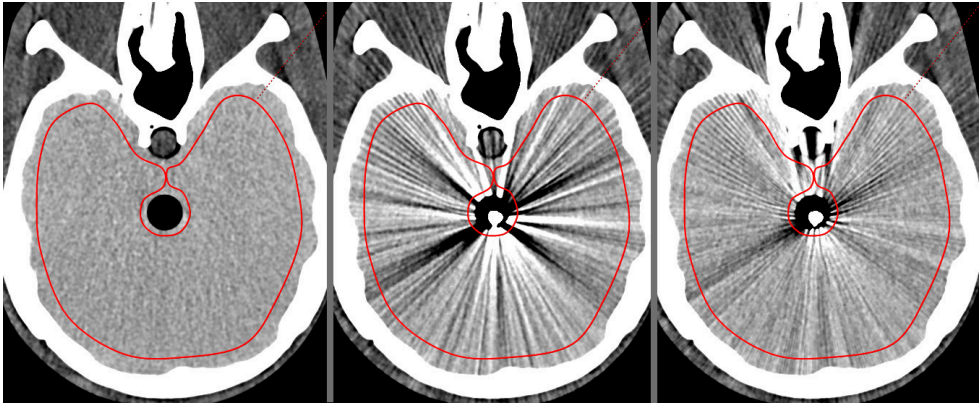


Figure 13.

Region-of-interest for quantitative image analysis. **Left:** reference, **middle:** with coils, **right:** with coils and metal artifact reduction algorithm. Adopted from **Paper IV**.

VGA was performed using images from both the phantom and clinical patient. Twelve reconstructions were included in the qualitative analysis: MI at 60, 80, 100, 120 and 140 keV, and PI, all with and without MAR. Four observers were asked to choose which two reconstructions they preferred regarding:

1. Overall image quality
2. Reduction of metal artifacts
3. Soft tissue differentiation in artifact afflicted regions
4. Soft tissue differentiation in the whole scan

First choice was awarded 2 points, and the second 1 point, to determine an overall superior reconstruction for each criterion.

Phantom images were assessed regarding only criteria 1-2, as there was no visible or measurable difference in HU for white matter and gray matter in the PI.

The observers then scored the images one at a time, using a four-point scale (1 – Non-diagnostic, 2 – Poor, 3 – Good, 4 – Excellent).

Results and discussion

Contributions to stroke imaging

The papers in this thesis highlight the role of spectral CT in advancing stroke imaging, primarily by enhancing contrast, reducing artifacts and introducing a potential new approach for perfusion assessment.

Brain perfusion

Perfusion imaging is central to identifying tissue at risk and guide stroke treatment decisions. A study comparing predictive models incorporating NCCT, CTA and CTP found that CTP provided the most accurate prediction of patient outcomes. However, since CTA was assessed visually for collateral scoring and occlusion status, the apparent superiority of CTP may partly stem from the absence of an objective, quantitative analysis of CTA images [84].

In **Paper I**, we introduced a quantitative method of analyzing mCTA images, using results from CTP as a guide. The lower temporal resolution of mCTA increases the risk of not perfectly capturing the arterial peak, potentially making perfusion assessments harder to perform. However, in terms of identifying brain regions affected by underperfusion, the mCTA method demonstrated similar results to CTP. Normal brain regions in patients with a detected perfusion deficit exhibited similar MVDs to those of patients with a normal perfusion (Figure 14)

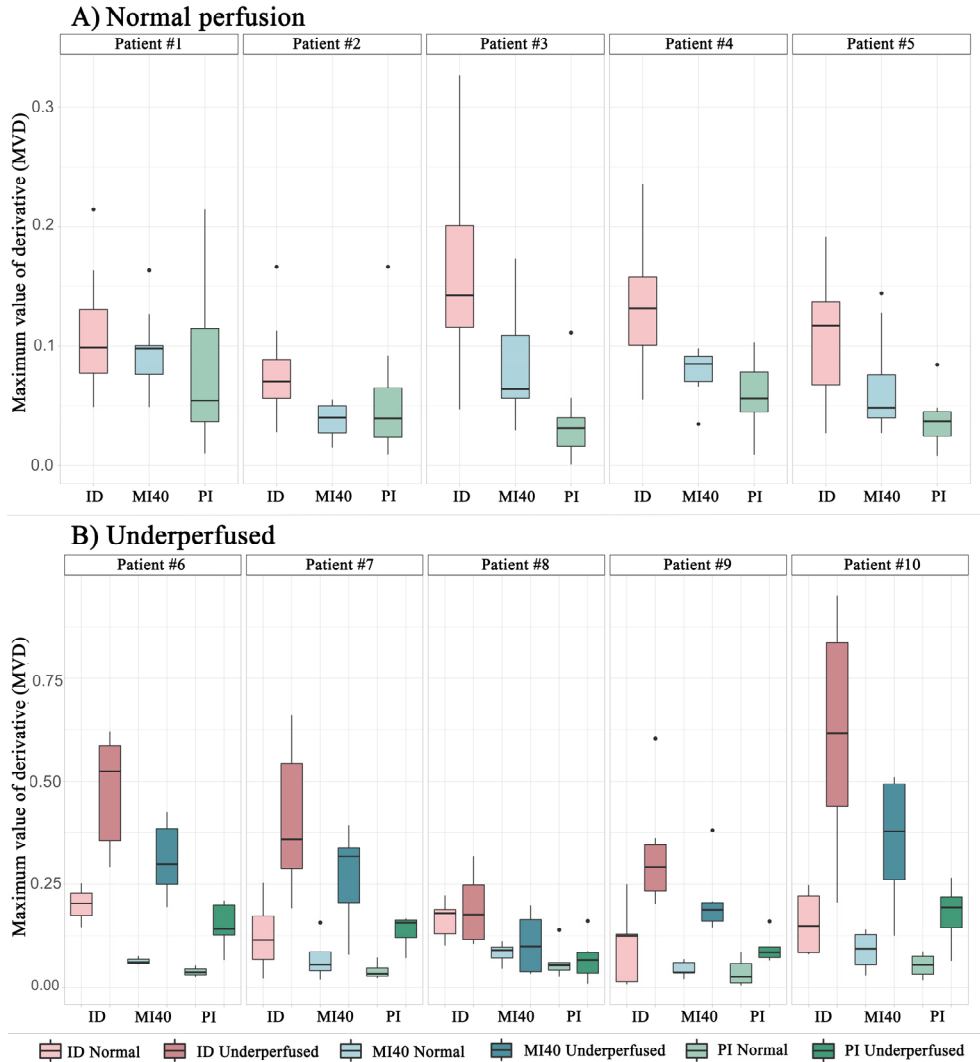


Figure 14.

A) Five patients with normal perfusion and **B)** five patients with underperfused regions, according to computed tomography perfusion (CTP). The maximum value of derivative (MVD) is presented for iodine density (ID), monoenergetic images at 40 keV (MI40) and polyenergetic images (PI). Patients #6 and #10 had an internal carotid occlusion. Patients #7 and #9 had an occlusion in the M1 segment and patient #8 in the M3 segment of the middle cerebral artery. Created using data from **Paper I**.

In contrast, regions with a perfusion deficit showed elevated MVDs compared to normal regions. Several other studies have also demonstrated the feasibility of quantitative mCTA as a potential substitute for CTP [85-88]. Compared to CTP, mCTA offers advantages, including direct visualization of arterial occlusions and

whole-brain coverage, which are not always available with CTP. Various methods of mCTA perfusion analysis have been proposed, with most relying on visual and/or quantitative hemispheric comparisons. Additionally, AI-based analysis of mCTA has shown high concordance with CTP perfusion maps [89, 90]. AI models offer an advantage over purely mathematical algorithms by integrating additional clinically relevant data, potentially enhancing the accuracy of predictions.

Our study found that ID and HU in MIs at 40 keV produced a clearer distinction between normal and underperfused tissue compared to PIs. Similarly, other research has demonstrated that MIs at 40 keV improve the identification of penumbra and ischemic core while offering better prediction of final infarct volume, both visually and through quantitative analysis [88].

The degree of underperfusion (volume and/or severity) influenced the capability of our proposed method. In images with large perfusion deficits (ICA occlusions in patient 6 and 10, Figure 14), there was a clear separation between MVDs of normal and underperfused tissue, while in images with more distal occlusions (M3 occlusion, patient 8) there was substantial overlap, reducing our method's effectiveness in distinguishing perfusion differences. Measurements were performed in large ROIs (Figure 10), making the method less sensitive to small perfusion deficits. A minor underperfusion within an otherwise well-perfused arterial territory is unlikely to have a strong influence on the average ROI value, limiting detectability. To enhance this method's sensitivity, future improvements could involve using smaller ROIs or performing the analysis at voxel level to generate perfusion maps, similar to conventional CTP.

Differentiation of gray and white matter

For any material, the change in attenuation as a result of change in MI level is most pronounced at low energies but becomes less noticeable at higher energies. Regardless of the specific imaging task, identifying a single optimal MI level is challenging, instead results typically indicate an energy range rather than a fixed value. Depending on study design and spectral CT solution, the optimal reconstruction for gray- and white matter differentiation has been reported to be MIs between 50 and 90 keV [17, 18, 91-94].

In **Paper II**, the CNR between gray matter (ischemic or normal) and white matter was maximized for MIs at 40 keV. Attenuation differences between ischemic and normal gray matter are due to cell death-induced edema, increasing water content and reducing attenuation. An unexpected finding was the low CNR between ischemic and gray matter for MIs at 40-50 keV, caused by negligible differences in attenuation. A

probable explanation for the high ischemic gray matter attenuation at low energies is the ROI placement (Figure 12). The ROI was placed cortically, making it susceptible to cupping artifacts caused by beam hardening from the cranial bone, which are amplified at low energies, while the ROI for normal gray matter was placed internally, shielded from such interference.

In the presence of metal devices, gray and white matter differentiation is further complicated by streak artifacts. Although artifacts are less pronounced at higher MI levels, **Paper IV** demonstrated that low-energy MIs (such as at 60 keV) remained the preferred choice when high soft tissue contrast is required, highlighting the trade-off between artifact reduction and soft tissue visibility.

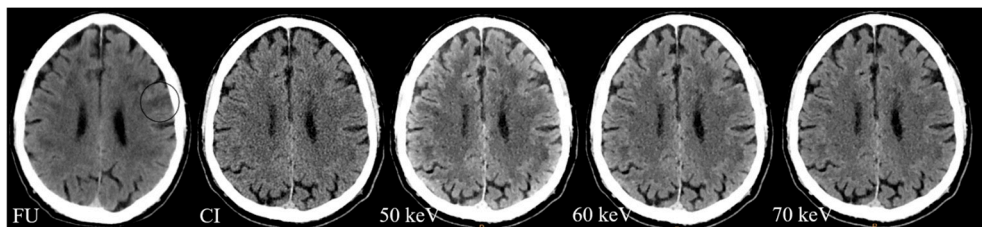


Figure 15.

Example images from a patient with an acute ischemic lesion, circled in the follow-up (FU) examination on the far left. Reconstructions for the acute examination are the conventional polyenergetic image (CI) and monoenergetic images at 50, 60 and 70 keV. Adopted from **Paper II**.

Diagnostic performance

In **Paper II**, we evaluated the diagnostic performance of two radiologists qualitatively detecting acute cortical ischemic lesion detection in PIs and MIs reconstructed from NCCT scans (Figure 15). Compared to the original diagnostic report, where the radiologists only had access to PIs, diagnostic accuracy was improved when they had access to MIs at 50, 60 and 70 keV alongside the PIs. Sensitivity increased from 0.55 to 0.93 and 0.97 for observers 1 and 2, respectively. However, this improvement came at the cost of decreased specificity, which declined from 1.0 to 0.82 and 0.91, respectively.

In contrast, another study in which observers evaluated one MI at a time reported a much lower sensitivity (best-performing MI was at 90 keV, 0.37) but slightly higher specificity (0.94) [94]. Their findings emphasized the importance of multiple observers, since inter-observer differences were larger than differences between reconstruction types. However, notably, each observer performed a more accurate evaluation with MIs than with PIs, reinforcing the value of spectral reconstructions. In our study, inter-

observer agreement was very good in terms of ischemia identification and localization, but only moderate when rating individual reconstructions. While MIs improve detection, variability remains when observers assess different reconstructions independently.

Assessing diagnostic performance requires a reliable reference standard. In **Paper II**, follow-up imaging (CT or MRI) was used as the ground truth. However, any misclassification of ischemic lesions or their location inevitably reduces the certainty of calculated diagnostic accuracy. Furthermore, the conditions under which images were reviewed in the original diagnostic report versus the visual grading sessions differed. During the visual grading sessions, observers were provided with clinical information from the referral report to improve realism. However, without access to previous radiological examinations, their ability to distinguish between old and acute lesions was limited, potentially impacting performance.

Superior reconstruction for ischemia localization

In **Paper II**, the MIs included in the visual grading were selected based on quantitative analysis results. Highest overall image quality was observed at 50 keV (rated “good” and “fair” by Observers 1 and 2) and 60 keV (rated “good” by both observers), with significantly higher scores compared to PIs. Similarly, for diagnostic ability, the highest ratings were given to MIs at 50 keV (“excellent” and “fair”) and 60 keV (“good”), while PIs were graded as “poor”. Across both image quality and diagnostic ability, MIs received significantly higher scores than PIs.

Regarding the preferred reconstruction for ischemia assessment, one observer selected the 60 keV MI in 28/52 cases, and the 50 keV MI in 19/52 cases. The other observer predominantly preferred PIs (35/52 cases), highlighting inter-observer variability despite overall superiority of MIs.

While gray-white matter contrast is maximized at the lowest MI levels, previous studies have suggested that MIs at 80-100 keV are optimal for ischemia assessment in regions suffering from beam hardening artifacts, such as the posterior fossa and subcalvarial space [93-95].

Arterial enhancement

The quantitative analysis in **Paper III** demonstrated that MIs reconstructed at 40-60 keV from Group 3 scans (half CM dose, optimized timing) exhibited significantly higher SNR and CNR compared to PIs from Group 1 (full CM dose). Additionally, the qualitative analysis found that MIs at 50 keV from Group 3 had significantly higher

overall image quality and improved visualization of the ICA and M2 artery (Figure 16.). However, while statistically significant, the observed difference was smaller than one graded scale level, suggesting it may not be clinically relevant. Therefore, we concluded that MIs from Group 3 were, at least, of equal quality to PIs from Group 1. This finding aligns with previous studies across different anatomical regions, which have shown that CM dose reductions of 25-50% can be effectively compensated by reconstructing MIs at 50-60 keV [19, 96-99].

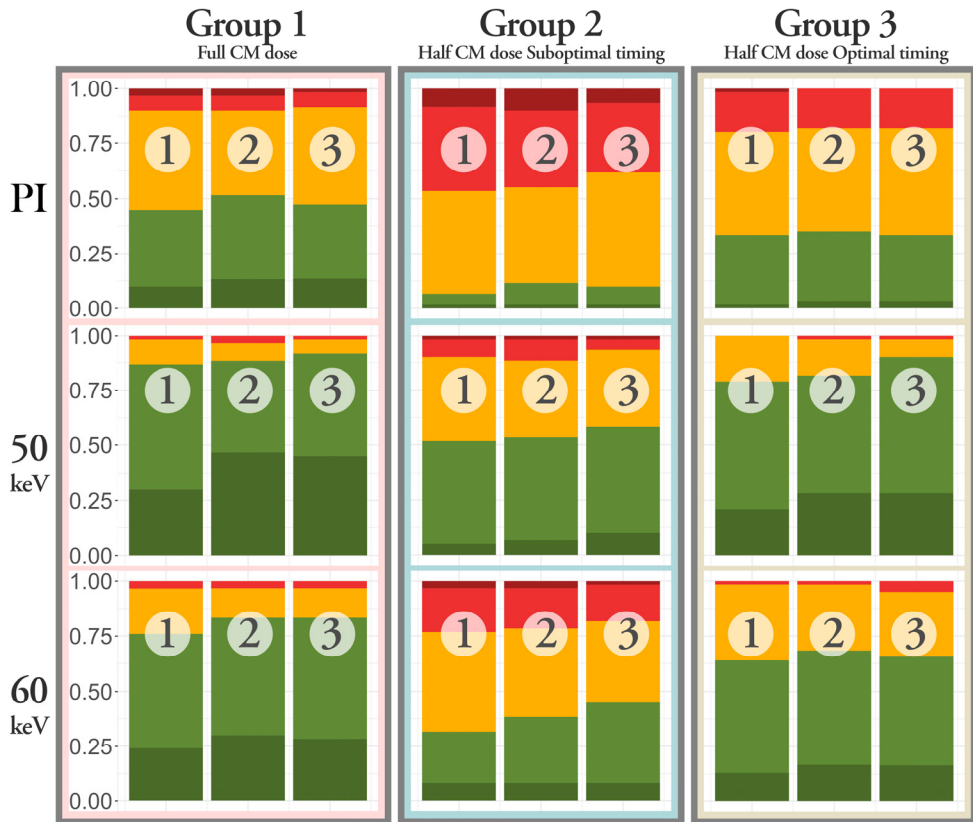


Figure 16. Score distribution for **1)** overall image quality, **2)** visual representation of the internal carotid artery, and **3)** visual representation of the M2 segment of the middle cerebral artery. Adopted from **Paper III**.

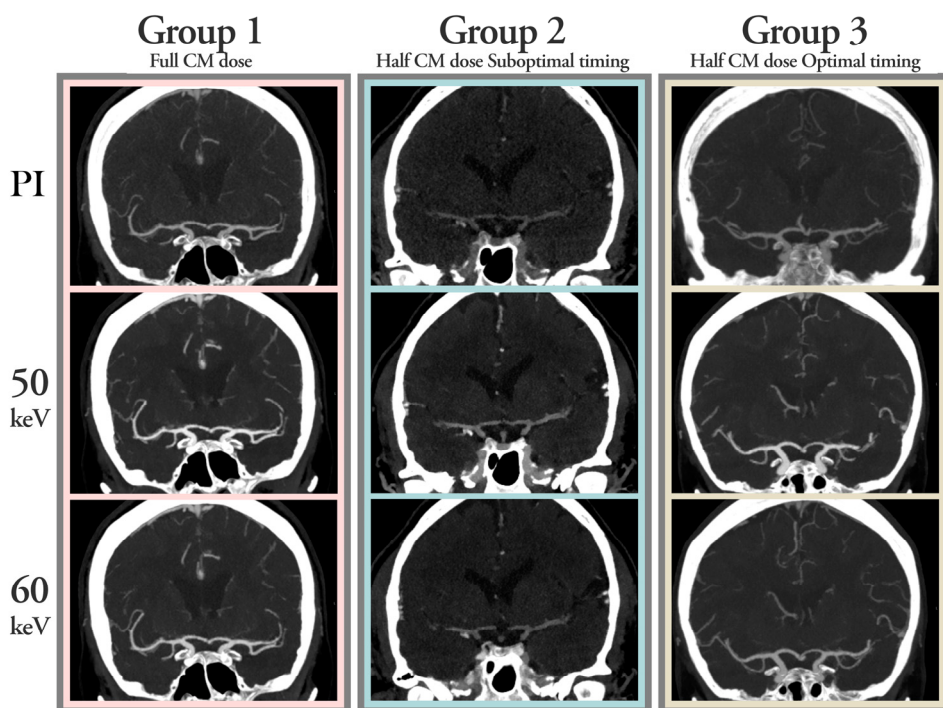


Figure 17.

Reconstructed polyenergetic images (PI), and monoenergetic images at 50 and 60 keV from patients in Groups 1-3. CM – Contrast medium. Adopted from **Paper III**.

Differences in scan parameters may have influenced our results. Group 3 images were acquired using a higher pitch than Groups 1 and 2, which could lower image quality, particularly in regions with high attenuation gradients. However, patients in Group 3 also received a slightly higher radiation dose, which – though statistically insignificant – can contribute to reduced image noise. Importantly, the difference in contrast phase between Groups 1 and 3 was negligible, whereas the difference between Groups 2 and 3 was significant, a key factor when interpreting the results.

In stroke imaging, the risk associated with delayed treatment far outweighs the potential risk of CIN. The clinical principle of *"neurons over nephrons"* underscores this prioritization. However, stroke patients often undergo CM-intensive interventional procedures following the initial CT scan and in subsequent days, motivating CM dose reduction when image quality can be preserved.

Beyond clinical benefits, reducing CM dose also has environmental advantages. Iodinated CM are excreted unchanged in urine and poorly removed by wastewater

treatment systems, contributing to water contamination. Thus, lower CM doses not only reduce the risk of CIN but also minimize environmental impact.

In **Paper I**, spectral imaging enhanced vascular attenuation and the ability to quantitatively distinguish between normal and underperfused tissue. The difference in MVD was more pronounced when measured in MIs at 40 keV and ID maps than in PIs (Figure 14).

Salvaging examinations with poor arterial enhancement

Contrast enhancement in CT imaging is influenced by multiple factors, and suboptimal contrast timing is a common challenge. For instance, for a hypothetical adult male (30 years old, 70 kg, 170 cm), a 60% reduction in cardiac output can cause a 30-second delay in peak aortic enhancement, shifting it from 30 to 60 seconds post CM-injection [100]. The prevalence of poorly-timed examinations varies depending on the body region and the criticality of the timing. A study by Mahmoudi et al. reported that 3.8% of 11,746 abdominal contrast-enhanced scans had poor contrast timing [101]. Of these, 36.9% (or 1.4% of all examinations), were considered non-diagnostic (rated “very poor” or “poor”) using the standard PIs. However, nearly all non-diagnostic cases in their study achieved acceptable image quality with MIs at 50 keV. Similarly, MIs at 40 keV from PCCT scans have been shown to enhance arterial contrast in venous-phase images, improving image quality though not to a level comparable with a true arterial-phase image [102].

In **Paper III**, among the poorly timed examinations (Group 2) – which also had a lower-than standard CM dose – the proportion of non-diagnostic (rated “poor” or lower) conventional PIs was lower than in the study by Mahmoudi et al. For overall image quality and ICA visualization, 10-12% of all images were rated “non-diagnostic” or “poor”. For M2 it was 19%. When using MIs at 50 keV, 69-79% were rated “fair” image quality, or better. Compared to the study by Mahmoudi et al, the proportion of examinations that were changed from non-diagnostic to fair using MIs was relatively low in our study, likely due to the added challenge of a reduced CM dose.

When MIs are reconstructed from poorly timed examinations with a standard CM dose, they can achieve diagnostic image quality. Our findings suggest that even with a 50% reduction in CM dose and suboptimal contrast timing, many examinations could still reach diagnostic quality.

Artifacts in brain imaging

Using MAR algorithms in combination with MIs is an interesting concept, as MAR algorithms were designed for PIs and may exhibit varying results depending on MI level. A previous study found no significant differences in assessed metal artifact severity between MI levels without using MAR [103]. However, regarding overall image quality and gray-white matter differentiation, MIs at 40 keV received the lowest scores, whereas MIs at 50 and 60 keV were rated highest.

During the VGA study in **Paper IV**, it was observed that applying MAR algorithms introduced new image disturbances, particularly in the more distal brain regions (Figure 18). This phenomenon has also been reported in other studies [104-106]. CT manufacturers recommend reconstructing images both with and without MAR, and our findings support this approach.

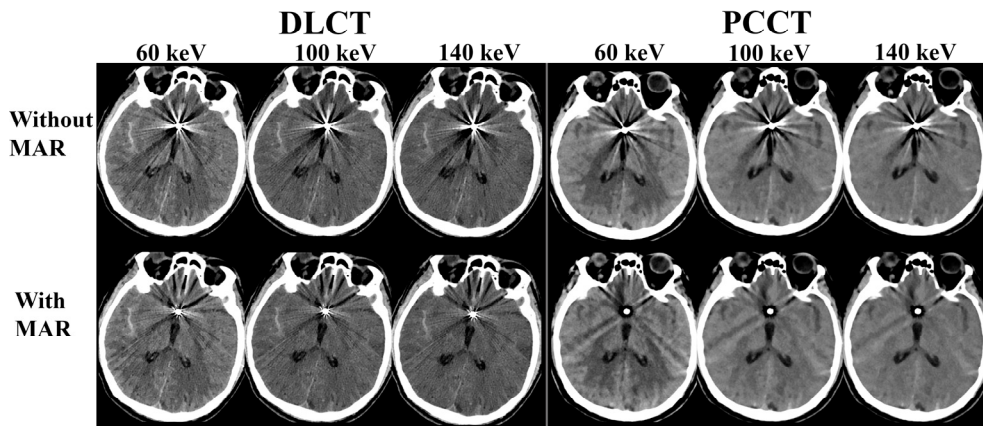


Figure 18. Patient images example for the dual layer computed tomography (DLCT, left) and photon counting computed tomography (PCCT, right). From left to right: monoenergetic image reconstructions at 60, 100 and 140 keV, top row without metal artifact reduction (MAR) and bottom row with MAR. Window settings were the same for both computed tomography systems (center=40, width=80). Adopted from **Paper IV**.

Metal artifact reduction

Both the qualitative and quantitative evaluations in **Paper IV** showed that MAR reduced artifact severity, across all MI and PI reconstructions and for both systems studied (Figure 19, Figure 20, Figure 21). Applying MAR had a greater impact on artifact severity than varying the MI level, though high-energy MIs were able to provide

further artifact reduction. Additionally, MIs offer advantages such as reduced sensitivity to beam hardening effects.

High-energy MIs generally exhibited minimal artifact severity, with some exceptions. For DLCT scans, the artifact index reached a minimum at 60 keV, while the minimum SD value was between 70-100 keV. These findings may be explained by the fact that MIs reconstructed at 70 keV from DLCT closely resemble conventional PIs, yet offer a lower noise level, making them more compatible with the MAR algorithm.

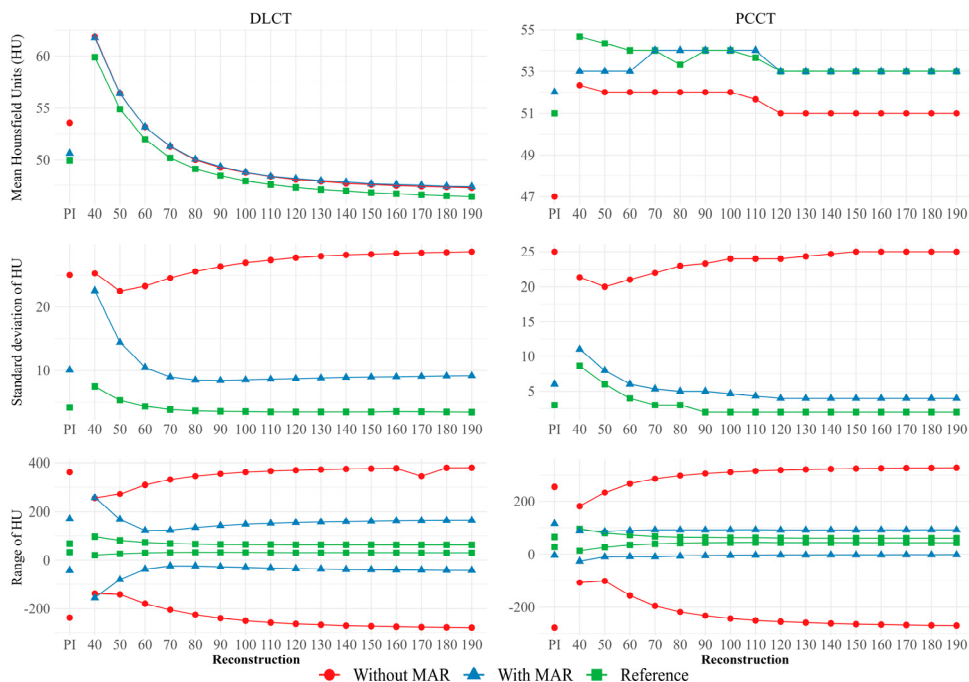


Figure 19.

Measured Hounsfield Units (HU), standard deviation and range (maximum and minimum HU) in polyenergetic images (PI) and monoenergetic images reconstructed at 40-190 keV, with and without metal artifact reduction (MAR), for a dual layer computed tomography (DLCT) and photon counting computed tomography (PCCT). Adopted from **Paper IV**.

During the qualitative image assessment in **Paper IV**, when observers compared multiple reconstructions simultaneously, the highest MI level studied (140 keV) was perceived to produce minimal artifacts. However, in absolute VGA, where images were assessed individually, artifact reduction scores varied only slightly across MI levels (median score range 3-3.5) (Figure 20). While high-energy MIs provided the greatest artifact reduction, the differences were subtle and difficult to detect in absolute VGA.



Figure 20.

Visual grading median score for patient images: polyenergetic image (PI) and monoenergetic images reconstructed at 60, 80, 100, 120 and 140 keV, with and without metal artifact reduction (MAR) on a dual layer computed tomography (DLCT, left) and photon counting computed tomography (PCCT, right). Adopted from **Paper IV**.

Score: 1 – Non-diagnostic, 2 – Poor, 3 – Good, 4 – Excellent.

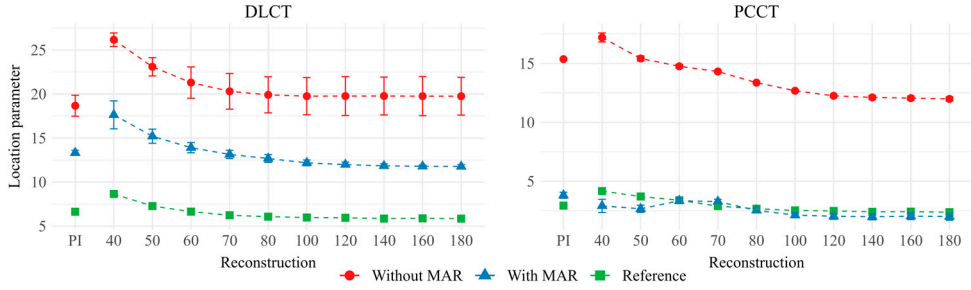


Figure 21.

The location parameter estimated from Gumbel distribution analysis in polyenergetic images (PI) and monoenergetic images reconstructed at 40-180 keV, with and without metal artifact reduction (MAR), for a dual layer CT (DLCT) and photon counting CT (PCCT). Adopted from **Paper IV**.

Overall image quality and soft tissue discrimination in the presence of metal artifacts

For overall image quality, when observers had access to all reconstructions simultaneously, reconstructions with MAR were consistently preferred. Regarding soft tissue discrimination, observers preferred MIs at lower energies without MAR, over MIs at higher energies with MAR. In contrast, when images were assessed individually, MAR had little impact on observer ratings across the different levels.

Observers rated MIs reconstructed at 60-80 keV and PIs higher than MI reconstructed at energies above 100 keV, presumably due to the improved soft tissue contrast at lower photon energies, which outweighed the benefits of artifact reduction at higher energies. This reinforces the importance of selecting MI level based on the specific diagnostic task. The quantitative analysis showed only slight improvements in artifact reduction beyond 80 keV, while qualitatively, soft tissue differentiation substantially worsened. Thus, MIs at 80 keV may provide a good trade-off between artifact reduction and soft tissue visualization.

Signal-to-noise ratio

In **Papers II-III**, SNR was used as a measure of image quality, comparing PIs and MIs. For soft tissue (gray or white matter), SNR was generally higher in MIs than in PIs (**Paper II**). For ischemic and normal gray matter, the difference was significant at 60-150 keV. For normal white matter, significance was only observed at 170-200 keV. Notably, SNR for ischemic gray matter and normal white matter was lower in MIs at 40 keV compared to PIs.

Theoretically, higher SNR in MIs results from reduced image noise since MIs experience less beam hardening and Compton scatter. However, similarly to SD, SNR interpretation in patient images can be complex. Despite efforts to measure in homogenous regions, anatomical variation is unavoidable. Image noise is expected to be greater at lower MI levels, but soft tissue differentiation is also enhanced. Both contribute to a higher SD, assuming non-homogenous tissue, and lower SNR, though only increased noise has a negative impact on image quality.

In contrast, the SNR behavior of arterial and venous segments in **Paper III** differed to that of soft tissue. SNR was highest at 40 keV and decreased with increasing MI level, with SNR in PIs closely resembling that of MIs at 80 keV. While SD varied similarly across MI levels in both vessels and soft tissues, the attenuation of iodinated vessels changed more dramatically with energy. As a result, SNR was primarily driven by iodine attenuation, peaking at lower photon energies where iodine attenuation is highest.

Contrast-to-noise ratio

The choice of background tissue for arterial CNR calculations should accurately represent its surrounding environment. Intracranial arteries are encased in a layer of fat, but in **Paper III**, white matter was used as the background tissue. The fat layer was not considered visible due to limited spatial resolution and calcium blooming artifacts. It was estimated that the arterial visualization depended more on contrast between the artery and white tissue rather than fat. If a higher spatial resolution was available, fat might be a more appropriate background tissue for CNR calculations.

Radiation dose considerations

Radiation doses for spectral CT are not necessarily higher than for conventional CT, though this depends on the specific spectral imaging solution. At Skåne University hospital in Lund, DLCT does not result in higher radiation doses compared to conventional single-energy CT.

Using PCCT can potentially reduce radiation dose substantially compared to DECT solutions, due to its ability to eliminate electronic noise and reduce overall noise levels. At Skåne University hospital in Lund, this advantage has been utilized for certain examinations particularly in pediatric imaging. However, in some cases, the higher

image quality of PCCT has been prioritized over dose reduction, maintaining radiation exposure comparable to conventional CT systems.

It is also important to note that radiation dose reductions may be limited in high-resolution imaging. The higher spatial resolution of PCCT inherently results in increased image noise, which can counteract the dose-saving potential. Currently, CTA of the neck and brain is performed at a radiation dose level similar to other CT systems, but with a significantly improved spatial resolution – achieving a 0.4 mm slice thickness (compared to 0.6 mm) and a 0.2 mm pixel size (compared to 0.6 mm). While this results in greater image detail, it also leads to higher noise levels compared to standard resolution CT.

The focus of this thesis was on maximizing the diagnostic utility of available spectral data, rather than optimizing radiation dose reduction. While minimizing radiation exposure is also desirable, it is not the primary concern in stroke imaging, where the risk of untreated ischemia far outweighs the potential risks associated with radiation.

In **Paper I**, we explored the possibility of substituting CTP with quantitative analysis of mCTA images, which – if implemented – would lead to a reduction in both CM and radiation dose, as it would eliminate the need to perform both mCTA and CTP.

We found in **Paper III** that many examinations with poor arterial enhancement could be improved from a non-diagnostic to diagnostic image quality, thereby eliminating the need to re-do the scan and reducing radiation exposure.

Limitations

The methodologies used in the papers of this thesis have inherent weaknesses, which may introduce limitations to the conclusions drawn.

Manual measurements

In **Papers I-IV**, manual quantitative measurements were performed, introducing potential risks of misplacement, partial volume effects and selection bias. However, our methodology maintained a level of objectivity when comparing different reconstructions (ID, PI or MIs) as a single ROI placement in one image automatically provided corresponding values for all reconstructions.

Imperfect standard bias

In **Paper I**, we aimed to develop a new method for perfusion assessment, which presented challenges regarding the choice of a reference standard. If the reference

standard is flawed or inaccurate, the new method will inherit bias from the reference, potentially affecting its perceived validity. By setting CTP results as ground truth, we limited our method to performing no better than CTP itself.

Statistical considerations

Sample sizes were determined based on previous studies and our research group's experience.

Paper I was a feasibility study, and the sample size was constrained by the time-consuming nature of manual ROI delineation.

Papers II and III were primarily limited in the qualitative analysis, as including multiple reconstructions per patient greatly increased observer workload. In **Paper III**, samples sizes were limited as we were unable to ethically justify continuing with a reduced CM dose protocol for additional patients without first confirming that image equality was adequately preserved.

In **Papers I and IV**, no statistical tests were performed due to the nature of the data and the small sample sizes. After consulting with our statistical advisor, we determined that statistical testing would not provide meaningful conclusions. Instead, we prioritized graphical representation of the data, ensuring transparency and interpretability while allowing for qualitative assessment of trends.

Visual grading analysis

To mitigate observer bias in VGA studies, we aimed to include observers with diverse background and experience levels.

In **Paper II**, two observers were recruited for each stage of the subjective analysis, which may be too few to ensure fully representative results. In **Paper III**, we increased the number of observers to four, allowing for a broader distribution of expertise and perspectives.

To enable unsupervised grading, we used dedicated software for VGA in **Papers II and III**. Achieving a high degree of realism is ideal for reviewing images. However, at the time of the study, the software only allowed for the presentation of a single image stack per case. More recent software versions now enable the simultaneous display of multiple image stacks, which would be an improvement. In **Paper IV**, supervised grading was found to be valuable, as it provided insights into the observers' thought processes. However, without a systematic approach to extract and analyze this information, it can only be considered anecdotal. Generally, the unsupervised approach is favored, as it is less time-consuming, allows observers greater flexibility in grading, and minimizes the risk of influence from the supervising researcher on the results.

Individual optimization of monoenergetic images

In this thesis, PIs and MIs were reconstructed using similar parameters whenever possible. However, optimizing reconstruction methods and filters for each reconstruction type could have further improved MI image quality. Optimizing the pre-set window may also improve perceived image quality [107]. While observers were able to adjust window settings during VGA studies, the extent to which they utilized this option was unknown.

Generalizability

Paper I-III were single-system studies, focused exclusively on DLCT, which limits the generalizability of the findings. The DLCT system was partly chosen for practical reasons, as it is available in the Skåne University Hospital neuroradiology department and serves as the designated stroke CT. This setup allowed for the retrospective analysis of many images without disrupting clinical workflow. In **Paper IV**, we expanded the analysis by comparing DLCT and PCCT, identifying both similarities and differences between the two systems. The parallel trends observed across both types of CT system suggest that our findings are more likely a property of MIs, rather than being system-specific.

Probability of benefit

The efficacy of diagnostic imaging can be understood as a hierarchical model of benefit probability, consisting of six levels [36, 108]:

- 1: **Technical quality** – Imaging parameters, image quality assessments
- 2: **Diagnostic accuracy** – Sensitivity, specificity
- 3: **Diagnostic thinking** – Degree to which imaging aids in diagnosis
- 4: **Therapeutic** – Degree to which imaging aids in treatment
- 5: **Patient outcome** – Change in outcome with vs without imaging
- 6: **Societal** – Cost-effectiveness from societal perspective

A study cannot demonstrate efficacy at a higher level without first establishing efficacy at the lower levels. **Papers I, III and IV** evaluated the technical quality (level 1), while **Paper II** also assessed the diagnostic accuracy (level 2). Thus, this thesis does not extend beyond level 2, meaning that we cannot draw conclusions as to whether spectral CT leads to improved patient outcome or is more cost-effective than conventional CT.

By modifying the study design, **Paper II** could have been expanded to include diagnostic thinking (level 3). This could have been achieved by conducting multiple reviewing sessions, where observers assessed the same cases with and without access to MIs. Such a setup would have allowed us to quantify the degree to which MIs aid diagnosis.

Conclusions

In brain CT imaging, the goal is to accurately visualize brain anatomy and function, recognize pathology and ensure that patients receive timely and appropriate diagnoses and treatment. To this goal, we investigated whether and how spectral CT can improve image quality in neuroradiological examinations typical for stroke imaging.

The conclusions from the individual papers are as follows:

- I. mCTA can be used for brain perfusion assessment. To improve the detection of perfusion deficits, the strongest possible iodine signal is preferred, which can be achieved using either direct iodine quantification or MIs reconstructed at 40 keV.
- II. The image quality of NCCT scans and consequently radiologists' ability to diagnose early ischemic lesions was improved using MIs at 50 and 60 keV compared to PIs. Diagnostic accuracy improved when radiologists had access to MIs, rather than relying solely on PIs.
- III. A 50% reduction in CM dose for CTA is feasible without compromising image quality when using MIs at 50 keV, compared to PIs with full CM dose. Alternatively, maintaining the CM dose while utilizing MIs can provide enhanced contrast and salvage examinations with poor arterial enhancement.
- IV. MIs reconstructed at energies ≥ 120 keV combined with MAR provided the lowest artifact severity in the presence of intracranial coils. However, for high soft tissue contrast, MIs at 60 keV were preferred. An intermediate energy such as 80 keV could be used for optimal balance. Since MAR can introduce new artifacts, reconstructions without MAR should always be included alongside MAR images.

The results presented in this thesis solidifies the importance of spectral CT in routine clinical practice. The use of spectral CT has been shown to enhance diagnostic image quality, compared to conventional polyenergetic imaging, across multiple types of neuroradiological CT examinations. Using quantitative analysis of images from spectral CT presents great potential for further clinical advancement.

Future perspectives

This thesis has demonstrated multiple ways in which spectral CT adds value in neuroradiology. Evaluating image quality through quantitative measures and VGA is straightforward, yet our ability to draw broader conclusions regarding benefit probability was limited. We therefore suggest that future studies should expand on evaluating both diagnostic performance and the therapeutic impact of spectral reconstructions.

Beyond its visual advantages, the quantitative capabilities of spectral CT are particularly promising. Spectral reconstructions facilitate functional imaging, allowing the identification of kidney stones, distinction between contrast extravasation and hemorrhage, and improved diagnosis and treatment evaluation in oncology [109-111]. Additionally, the use of CTA for perfusion imaging enables perfusion assessment in settings where traditional CTP is impractical, such as angiography suites or mobile CT units. Further research should focus on refining and validating these methods.

Spectral CT also has potential for proactive stroke prevention. Its ability to differentiate tissue composition can be applied to carotid plaque characterization, distinguishing stable asymptomatic plaques from high-risk plaques prone to rupture and stroke [112-114]. This is especially relevant with PCCT, which provides higher spatial resolution, enhancing the detection and assessment of vulnerable plaques.

Spectral CT is increasingly proving itself as a powerful and versatile imaging tool. Using PCCT can improve both spatial and spectral resolution while simultaneously reducing radiation dose. This may be particularly relevant as the increased utility of spectral CT could lead to broader use and more frequent CT examinations.

Another key area of advancement is the integration of AI across all aspects of diagnostic imaging, from spectral data analysis, image acquisition, reconstruction and pathology detection. As these technologies continue to evolve, spectral CT is poised to become an even more important part of advanced medical imaging.

Författarens tack

Jag har många personer att tacka för att jag kommit så här långt! Ett stort tack till mina handledare, som stöttat mig på olika sätt men alla varit lika oumbärliga.

Min huvudhandledare **Anders Tingberg** för att du trodde på mig och gav mig den här chansen. Tack för goda råd, stöttning och för att du alltid tar dig tid.

Min biträdande handledare, **Kristina Ydström**, för att du värvade mig till röntgendiagnostiken och delade med dig av din kärlek för teknik och forskning.

Min biträdande handledare, **Johan Wassélius**, för din medryckande entusiasm, otaliga forskningsförslag och förmåga att få ord och idéer till handling.

Tack till alla patienter vars undersökningsbilder gjort denna avhandling möjlig.

Tack till Region Skåne som till stor del finansierat och möjliggjort detta arbete. Tack till **Per Munck af Rosenschöld** och **Silke Engelholm** för möjligheten att kombinera mitt kliniska arbete med doktorandstudier.

Tack till vänner och kollegor på Medicinsk strålningsfysik i Malmö, Lunds universitet, samt på Strålningsfysik och Bild- och funktion, Skånes Universitetssjukhus.

Stroke Imaging Group och mina medförfattare som bidragit med expertis, tid och stöd. Tack **Birgitta Ramgren**, **Francesco Arena**, **Mattias Drake**, **Teresa Ullberg** och **Per Undrén** för era betydelsefulla bidrag i bildgranskningen.

Speciellt tack till mina doktorandkollegor i datortomografi-forskningen, **Helena Mellander Oxholm** (numera doktor!) och **Henrik Andersson**, för allt samarbete och allt jag fått lära mig från er.

Mina Lunda-kollegor! Tack för att ni gör jobbet kul att gå till. **Fredrik Wellman**, **Inga Göransson**, **Marie-Louise Aurumskjöld**, **Pontus Timberg**.

Nuvarande och dåvarande kollegor i hela regionen. **Christian Andersson**, **Hannie Förnvik**, **Marcus Söderberg**, **Martin Eckerwall**, **Mikael Gunnarsson**, **Veronica Nilsson Lindström**, **Johan Olsrud**, **Johan Tano**, **Bea Jutemark Kvam**, **Sven Månsson**.

Susann Ullén och **Sara Jespersen** för goda råd om statistiska analyser. Thanks to **Lee Nolan** for expert language editing of manuscripts and thesis summary.

Tack till mina vänner och familj!

Mina klasskamrater från sjukhusfysikerprogrammet! Tillsammans blev vi lite klokare varje dag och utan den grunden hade jag inte vågat fortsätta på det akademiska spåret. **Andrea Fingerhut, Fanny Mörnjö Centofanti, Frida Westerbergh, Sajad Mohammed Ali, Tobias Rosholm, Tra Pham, Victor Pham.**

Anna Bjerkén, Hanna Tomic och Petter Wilke, som jag fått förmånen att ha som kollegor även efter examen.

Beatrice Akinrimisi, för att du erbjöd dig att bli min familj i Skåne och aldrig har tvekat att ställa upp.

Tack till **Matilda, Linnéa och Charlotte**, för långa samtal som gjort att ni alltid känts nära även när vi varit separerade av land eller oceaner.

Tack till **Andreas**, för alla glada stunder och stöd under studieåren.

Min **mamma Barbro**, som alltid trott på mig och att jag kan nå alla mina mål.

Min **pappa Kenneth**, som lärt mig att fira framgångar och ta lärdom av motgångar.

Ida, Anna och Nathalie, man väljer inte sina systrar men er hade jag valt 100 gånger om! Jag är så glad att ha er, och att våra barn har en sådan härlig kusinflock att växa upp i.

Farmor Kerstin, tack för att du är en varm och vänlig plats, för att du lärt mig att se livet från den ljusa sidan och vara glad för det jag har.

Och till sist dem som betyder allra mest. Tack **Tyr** och **Ponyo** för allt gos och bus som livet med barn och hund bjuder på. Tack **Niklas** – jag älskar dig och är så stolt över dig och allt vi gjort tillsammans hittills, och jag ser fram emot allt som väntar.

References

1. Pu, L., et al., Projected Global Trends in Ischemic Stroke Incidence, Deaths and Disability-Adjusted Life Years From 2020 to 2030. *Stroke*, 2023. **54**(5): p. 1330-1339.
2. Hounsfield, G.N., Computerized transverse axial scanning (tomography). 1. Description of system. *Br J Radiol*, 1973. **46**(552): p. 1016-22.
3. Hsieh, J. and T. Flohr, Computed tomography recent history and future perspectives. *J Med Imaging (Bellingham)*, 2021. **8**(5): p. 052109.
4. Flohr, T.G., et al., First performance evaluation of a dual-source CT (DSCT) system. *European Radiology*, 2006. **16**(2): p. 256-268.
5. Johnson, T.R.C., et al., Material differentiation by dual energy CT: initial experience. *European Radiology*, 2007. **17**(6): p. 1510-1517.
6. Rajendran, K., et al., First Clinical Photon-counting Detector CT System: Technical Evaluation. *Radiology*, 2022. **303**(1): p. 130-138.
7. McCollough, C.H., et al., Clinical applications of photon counting detector CT. *Eur Radiol*, 2023.
8. Kimpe, T. and T. Tuytschaever, Increasing the number of gray shades in medical display systems--how much is enough? *J Digit Imaging*, 2007. **20**(4): p. 422-32.
9. Dance, D.R., Christofides, S., Maidment, A. D.A., McLean, I. D., and Ng, K. H., Diagnostic radiology physics: A handbook for teachers and students. Endorsed by: American Association of Physicists in Medicine, Asia-Oceania Federation of Organizations for Medical Physics, European Federation of Organisations for Medical Physics. 2014: IAEA.
10. Hallstadius, L.H., S., Joniserande strålnings växelverkan med materia, L.U. Radiofysiska Institutionen, Editor. 1984: Lund.
11. Bushberg, J.T., et al., The essential physics of medical imaging. 2021, Wolters Kluwer: Philadelphia.
12. McCollough, C.H., et al., Dual- and Multi-Energy CT: Principles, Technical Approaches, and Clinical Applications. *Radiology*, 2015. **276**(3): p. 637-53.
13. Alkadhi, H., Spectral imaging : dual-energy, multi-energy and photon-counting CT. *Medical Radiology - Diagnostic Imaging*. 2022, Cham, Switzerland: Springer Nature Switzerland AG.

14. Lehmann, L.A., et al., Generalized image combinations in dual KVP digital radiography. *Medical Physics*, 1981. **8**(5): p. 659-667.
15. Liu, X., et al., Quantitative imaging of element composition and mass fraction using dual-energy CT: three-material decomposition. *Med Phys*, 2009. **36**(5): p. 1602-9.
16. Verdun, F.R., et al., Image quality in CT: From physical measurements to model observers. *Physica Medica*, 2015. **31**(8): p. 823-843.
17. Pomerantz, S.R., et al., Virtual monochromatic reconstruction of dual-energy unenhanced head CT at 65-75 keV maximizes image quality compared with conventional polychromatic CT. *Radiology*, 2013. **266**(1): p. 318-25.
18. Neuhaus, V., et al., Improvement of Image Quality in Unenhanced Dual-Layer CT of the Head Using Virtual Monoenergetic Images Compared With Polyenergetic Single-Energy CT. *Invest Radiol*, 2017. **52**(8): p. 470-476.
19. Rotzinger, D.C., et al., Reduced-iodine-dose dual-energy coronary CT angiography: qualitative and quantitative comparison between virtual monochromatic and polychromatic CT images. *Eur Radiol*, 2021. **31**(9): p. 7132-7142.
20. Pan, Y.-N., et al., Reduction of Metallic Artifacts of the Post-treatment Intracranial Aneurysms: Effects of Single Energy Metal Artifact Reduction Algorithm. *Clinical Neuroradiology*, 2019. **29**(2): p. 277-284.
21. Lehti, L., et al., Iterative metal artifact reduction in aortic CTA after Onyx®-embolization. *European Journal of Radiology Open*, 2020. **7**.
22. Mellander, H., et al., Metal artifact reduction by virtual monoenergetic reconstructions from spectral brain CT. *European Journal of Radiology Open*, 2023. **10**.
23. Meyer, E., et al., Normalized metal artifact reduction (NMAR) in computed tomography. 2009 IEEE Nuclear Science Symposium Conference Record (NSS/MIC), 2009: p. 3251-3255.
24. Philips White Paper, Metal Artifact Reduction for Orthopedic Implants (O-MAR), P. Healthcare, Editor. 2012.
25. Meyer, E., et al., Frequency split metal artifact reduction (FSMAR) in computed tomography. *Medical Physics*, 2012. **39**(4): p. 1904-1916.
26. Pal, D.D., S., K. Procknow, and J. Hsieh, GE White Paper, Smart Metal Artifact Reduction (MAR), G. Healthcare, Editor. 2016.
27. Imai, K., et al., Analysis of streak artefacts on CT images using statistics of extremes. *British Journal of Radiology*, 2014. **80**(959): p. 911-918.
28. Nomura, Y., et al., Evaluation of streak metal artifacts in cone beam computed tomography by using the Gumbel distribution: a phantom study. *Oral Surgery, Oral Medicine, Oral Pathology and Oral Radiology*, 2021. **131**(4): p. 494-502.

29. Ishikawa, T., et al., Metal artifacts reduction in computed tomography: A phantom study to compare the effectiveness of metal artifact reduction algorithm, model-based iterative reconstruction, and virtual monochromatic imaging. *Medicine (Baltimore)*, 2020. **99**(50): p. e23692.
30. Månsson, L.G., Methods for the Evaluation of Image Quality: A Review. *Radiation Protection Dosimetry*, 2000. **90**(1-2): p. 89-99.
31. Ludewig, E., A. Richter, and M. Frame, Diagnostic imaging--evaluating image quality using visual grading characteristic (VGC) analysis. *Vet Res Commun*, 2010. **34**(5): p. 473-9.
32. Tesselaar, E., N. Dahlström, and M. Sandborg, Clinical audit of image quality in radiology using visual grading characteristics analysis. *Radiat Prot Dosimetry*, 2016. **169**(1-4): p. 340-6.
33. Precht, H., et al., Radiographers' perspectives' on Visual Grading Analysis as a scientific method to evaluate image quality. *Radiography (Lond)*, 2019. **25 Suppl 1**: p. S14-s18.
34. Shrimpton, P.P., W. Jessen, K., European Guidelines on quality criteria for Computed Tomography. 2000.
35. Obuchowski, N.A., Special Topics III: Bias. *Radiology*, 2003. **229**(3): p. 617-621.
36. Sica, G.T., Bias in Research Studies. *Radiology*, 2006. **238**(3): p. 780-789.
37. Löve, A., Optimization of image quality and radiation dose in neuroradiological computed tomography, in Lund University Faculty of Medicine Doctoral Dissertation Series. 2013, Diagnostic Radiology, (Lund), Lund University. p. 98.
38. Börjesson, S., et al., A software tool for increased efficiency in observer performance studies in radiology. *Radiat Prot Dosimetry*, 2005. **114**(1-3): p. 45-52.
39. Håkansson, M., et al., VIEWDEX: an efficient and easy-to-use software for observer performance studies. *Radiat Prot Dosimetry*, 2010. **139**(1-3): p. 42-51.
40. Svåkvist, A., et al., ViewDex 3.0 - Recent development of a software application facilitating assessment of image quality and observer performance. *Radiat Prot Dosimetry*, 2021. **195**(3-4): p. 372-377.
41. Båth, M. and L.G. Månsson, Visual grading characteristics (VGC) analysis: a non-parametric rank-invariant statistical method for image quality evaluation. *Br J Radiol*, 2007. **80**(951): p. 169-76.
42. Hansson, J., L.G. Månsson, and M. Båth, The validity of using ROC software for analysing visual grading characteristics data: An investigation based on the novel software VGC Analyzer. *Radiat Prot Dosimetry*, 2016. **169**(1-4): p. 54-9.
43. Båth, M. and J. Hansson, VGC Analyzer: A software for statistical analysis of fully crossed multiple-reader multiple-case visual grading characteristics studies. *Radiat Prot Dosimetry*, 2016. **169**(1-4): p. 46-53.

44. Hansson, J., L.G. Månsson, and M. Båth, Evaluation of VGC Analyzer by comparison with gold standard ROC software and analysis of simulated visual grading data. *Radiat Prot Dosimetry*, 2021. **195**(3-4): p. 378-390.
45. Birkelo, C.C., W.E. Chamberlain, and et al., Tuberculosis case finding; a comparison of the effectiveness of various roentgenographic and photofluorographic methods. *J Am Med Assoc*, 1947. **133**(6): p. 359-66.
46. Cohen, J., A Coefficient of Agreement for Nominal Scales. *Educational and Psychological Measurement*, 1960. **20**: p. 37 - 46.
47. Altman, D.G., *Practical statistics for medical research*. 1991, London, UK: Chapman & Hall/CRC.
48. McHugh, M.L., Interrater reliability: the kappa statistic. *Biochem Med (Zagreb)*, 2012. **22**(3): p. 276-82.
49. Hacke, W., et al., Thrombolysis with alteplase 3 to 4.5 hours after acute ischemic stroke. *N Engl J Med*, 2008. **359**(13): p. 1317-29.
50. Wintermark, M., et al., Imaging recommendations for acute stroke and transient ischemic attack patients: A joint statement by the American Society of Neuroradiology, the American College of Radiology, and the Society of NeuroInterventional Surgery. *AJNR Am J Neuroradiol*, 2013. **34**(11): p. E117-27.
51. Powers, W.J., et al., 2018 Guidelines for the Early Management of Patients With Acute Ischemic Stroke: A Guideline for Healthcare Professionals From the American Heart Association/American Stroke Association. *Stroke*, 2018. **49**(3): p. e46-e110.
52. Jauch, E.C., et al., Guidelines for the early management of patients with acute ischemic stroke: a guideline for healthcare professionals from the American Heart Association/American Stroke Association. *Stroke*, 2013. **44**(3): p. 870-947.
53. Barber, P.A., et al., Imaging of the brain in acute ischaemic stroke: comparison of computed tomography and magnetic resonance diffusion-weighted imaging. *J Neurol Neurosurg Psychiatry*, 2005. **76**(11): p. 1528-33.
54. Wardlaw, J.M. and O. Mielke, Early signs of brain infarction at CT: observer reliability and outcome after thrombolytic treatment--systematic review. *Radiology*, 2005. **235**(2): p. 444-53.
55. Barber, P.A., et al., Validity and reliability of a quantitative computed tomography score in predicting outcome of hyperacute stroke before thrombolytic therapy. ASPECTS Study Group. Alberta Stroke Programme Early CT Score. *Lancet*, 2000. **355**(9216): p. 1670-4.
56. Chung, K.J., D. De Sarno, and T.-Y. Lee, Quantitative functional imaging with CT perfusion: technical considerations, kinetic modeling, and applications. *Frontiers in Physics*, 2023. **11**.
57. Wassélius, J., et al., Endovascular thrombectomy for acute ischemic stroke. *J Intern Med*, 2022. **291**(3): p. 303-316.

58. Menon, B.K., et al., Multiphase CT Angiography: A New Tool for the Imaging Triage of Patients with Acute Ischemic Stroke. *Radiology*, 2015. 275(2): p. 510-20.
59. Yu, A.Y., et al., Multiphase CT angiography increases detection of anterior circulation intracranial occlusion. *Neurology*, 2016. 87(6): p. 609-16.
60. Reid, M., et al., Accuracy and Reliability of Multiphase CTA Perfusion for Identifying Ischemic Core. *Clin Neuroradiol*, 2019. 29(3): p. 543-552.
61. Wang, C.L., et al., Frequency, outcome, and appropriateness of treatment of nonionic iodinated contrast media reactions. *AJR Am J Roentgenol*, 2008. 191(2): p. 409-15.
62. Kagan, A. and D. Sheikh-Hamad, Contrast-induced kidney injury: focus on modifiable risk factors and prophylactic strategies. *Clin Cardiol*, 2010. 33(2): p. 62-6.
63. Rudnick, M.R., et al., The Controversy of Contrast-Induced Nephropathy With Intravenous Contrast: What Is the Risk? *Am J Kidney Dis*, 2020. 75(1): p. 105-113.
64. Shams, E. and H.N. Mayrovitz, Contrast-Induced Nephropathy: A Review of Mechanisms and Risks. *Cureus*, 2021. 13(5): p. e14842.
65. Hossain, M.A., et al., Contrast-induced nephropathy: Pathophysiology, risk factors, and prevention. *Saudi J Kidney Dis Transpl*, 2018. 29(1): p. 1-9.
66. Waaijer, A., et al., Circle of Willis at CT angiography: dose reduction and image quality--reducing tube voltage and increasing tube current settings. *Radiology*, 2007. 242(3): p. 832-9.
67. Björkdahl, P. and U. Nyman, Using 100- instead of 120-kVp computed tomography to diagnose pulmonary embolism almost halves the radiation dose with preserved diagnostic quality. *Acta Radiol*, 2010. 51(3): p. 260-70.
68. Kanematsu, M., et al., Low-Iodine-Load and Low-Tube-Voltage CT Angiographic Imaging of the Kidney by Using Bolus Tracking with Saline Flushing. *Radiology*, 2015. 275(3): p. 832-40.
69. Lehti, L., et al., 80-kVp CT angiography for endovascular aneurysm repair follow-up with halved contrast medium dose and preserved diagnostic quality. *Acta Radiol*, 2016. 57(3): p. 279-86.
70. Little, M.P., et al., Risks associated with low doses and low dose rates of ionizing radiation: why linearity may be (almost) the best we can do. *Radiology*, 2009. 251(1): p. 6-12.
71. Boice, J.D., Jr., The linear nonthreshold (LNT) model as used in radiation protection: an NCRP update. *Int J Radiat Biol*, 2017. 93(10): p. 1079-1092.
72. Shore, R.E., et al., Recent Epidemiologic Studies and the Linear No-Threshold Model For Radiation Protection-Considerations Regarding NCRP Commentary 27. *Health Phys*, 2019. 116(2): p. 235-246.
73. ICRP 1991. 1990 Recommendations of the International Commission on Radiological Protection. ICRP Publication 60. *Ann. ICRP* 21 (1-3).

74. ICRP 2007. Recommendations of the International Commission on Radiological Protection. ICRP Publication 103. Ann. ICRP 37 (2-4).
75. Almén, A.J., Lars, Radiologiska undersökningar i Sverige under 2018 (2020:14). 2020, SSM.
76. ICRP, 2000. Managing Patient Dose in Computed Tomography. ICRP Publication 87. Ann. ICRP 30 (4).
77. ICRP, 2007. Managing Patient Dose in Multi-Detector Computed Tomography (MDCT). ICRP Publication 102. Ann. ICRP 37 (1)
78. International Electrotechnical Commission (IEC), 2009. Medical electrical equipment. Part 2-44: Particular requirements for basic safety and essential performance of X-ray equipment for computed tomography. IEC 60691-2-44. Third edn.
79. Strauss, K., et al., Size Specific Dose Estimates in Pediatric and Adult Body CT Examinations, AAPM Task Group 2014. 2011.
80. McCollough, C., et al., Use of Water Equivalent Diameter for Calculating Patient Size and Size-Specific Dose Estimates (SSDE) in CT: The Report of AAPM Task Group 220. AAPM Rep, 2014. **2014**: p. 6-23.
81. Boone, J.M., et al., Size Specific Dose Estimate (SSDE) for Head CT: The Report of AAPM Task Group 293. AAPM Rep, 2019. **2019**.
82. Huda, W., D. Magill, and W. He, CT effective dose per dose length product using ICRP 103 weighting factors. Med Phys, 2011. **38**(3): p. 1261-5.
83. Demeestere, J., et al., Alberta Stroke Program Early CT Score Versus Computed Tomographic Perfusion to Predict Functional Outcome After Successful Reperfusion in Acute Ischemic Stroke. Stroke, 2018. **49**(10): p. 2361-2367.
84. Bivard, A., et al., Assessing the Relative Value of CT Perfusion Compared to Non-contrast CT and CT Angiography in Prognosticating Reperfusion-Eligible Acute Ischemic Stroke Patients. Frontiers in Neurology, 2021. **12**.
85. Chung, K.J., et al., Feasibility of deconvolution-based multiphase CT angiography perfusion maps in acute ischemic stroke: Simulation and concordance with CT perfusion. Journal of Stroke and Cerebrovascular Diseases, 2022. **31**(12): p. 106844.
86. Chung, K.J., et al., Multiphase CT angiography perfusion maps for predicting target mismatch and ischemic lesion volumes. Scientific Reports, 2023. **13**(1): p. 21976.
87. Duprez, T., et al., Preliminary experience of CT imaging of the ischaemic brain penumbra through spectral processing of multiphasic CTA datasets. Scientific Reports, 2023. **13**(1): p. 11431.
88. Aludin, S., et al., Spectral imaging and analysis of monophasic CT angiography to assess infarct core and penumbra in acute stroke. Scientific Reports, 2024. **14**(1): p. 28397.
89. Qiu, W., et al., Automated Prediction of Ischemic Brain Tissue Fate from Multiphase Computed Tomographic Angiography in Patients with Acute Ischemic Stroke Using Machine Learning. J Stroke, 2021. **23**(2): p. 234-243.

90. Cai, Y., et al. Masked Residual Diffusion Probabilistic Model with Regional Asymmetry Prior for Generating Perfusion Maps from Multi-phase CTA. 2024. Cham: Springer Nature Switzerland.
91. Lennartz, S., et al., Dual-layer detector CT of the head: Initial experience in visualization of intracranial hemorrhage and hypodense brain lesions using virtual monoenergetic images. *European Journal of Radiology*, 2018. **108**: p. 177-183.
92. Ståhl, F., et al., Performance of dual layer dual energy CT virtual monoenergetic images to identify early ischemic changes in patients with anterior circulation large vessel occlusion. *Journal of Neuroradiology*, 2021. **48**(2): p. 75-81.
93. Dodig, D., et al., Virtual monoenergetic dual-energy CT reconstructions at 80 keV are optimal non-contrast CT technique for early stroke detection. *Neuroradiol J*, 2022. **35**(3): p. 337-345.
94. van Ommen, F., et al., Virtual monochromatic dual-energy CT reconstructions improve detection of cerebral infarct in patients with suspicion of stroke. *Neuroradiology*, 2021. **63**(1): p. 41-49.
95. Hixson, H.R., et al., Utilizing dual energy CT to improve CT diagnosis of posterior fossa ischemia. *J Neuroradiol*, 2016. **43**(5): p. 346-52.
96. Carrascosa, P., et al., Monochromatic image reconstruction by dual energy imaging allows half iodine load computed tomography coronary angiography. *Eur J Radiol*, 2015. **84**(10): p. 1915-20.
97. Shuman, W.P., et al., Dual-energy CT Aortography with 50% Reduced Iodine Dose Versus Single-energy CT Aortography with Standard Iodine Dose. *Acad Radiol*, 2016. **23**(5): p. 611-8.
98. Johansen, C.B., et al., The potential of iodinated contrast reduction in dual-energy CT thoracic angiography; an evaluation of image quality. *Radiography (Lond)*, 2022. **28**(1): p. 2-7.
99. Higashigaito, K., et al., CT Angiography of the Aorta Using Photon-counting Detector CT with Reduced Contrast Media Volume. *Radiology: Cardiothoracic Imaging*, 2023. **5**(1): p. e220140.
100. Bae, K.T., Intravenous Contrast Medium Administration and Scan Timing at CT: Considerations and Approaches. *Radiology*, 2010. **256**(1): p. 32-61.
101. Mahmoudi, S., et al., Salvaging low contrast abdominal CT studies using noise-optimised virtual monoenergetic image reconstruction. *BJR|Open*, 2022. **4**(1).
102. Dillinger, D., et al., Optimizing Arterial Vessel Contrast in Portal Venous Phase with Virtual Monoenergetic Images from Photon-Counting Detector CT Scans of the Abdomen—First Clinical Experiences. *Diagnostics*, 2024. **14**: p. 627.
103. Mellander, H., et al., Metal artifact reduction by virtual monoenergetic reconstructions from spectral brain CT. *European Journal of Radiology Open*, 2023. **10**: p. 100479.

104. Zopfs, D., et al., Virtual monoenergetic images and post-processing algorithms effectively reduce CT artifacts from intracranial aneurysm treatment. *Sci Rep*, 2020. **10**(1): p. 6629.
105. Fitsiori, A., et al., Iterative Algorithms Applied to Treated Intracranial Aneurysms. *Clinical Neuroradiology*, 2019. **29**(4): p. 741-749.
106. Große Hokamp, N., et al., Reduction of Artifacts Caused by Deep Brain Stimulating Electrodes in Cranial Computed Tomography Imaging by Means of Virtual Monoenergetic Images, Metal Artifact Reduction Algorithms, and Their Combination. *Investigative Radiology*, 2018. **53**(7): p. 424-431.
107. Fu, W., et al., Optimizing window settings for improved presentation of virtual monoenergetic images in dual-energy computed tomography. *Med Phys*, 2017. **44**(11): p. 5686-5696.
108. Fryback, D.G. and J.R. Thornbury, The Efficacy of Diagnostic Imaging. *Medical Decision Making*, 1991. **11**(2): p. 88-94.
109. Andersen, M.B., et al., Impact of spectral body imaging in patients suspected for occult cancer: a prospective study of 503 patients. *Eur Radiol*, 2020. **30**(10): p. 5539-5550.
110. Drljevic-Nielsen, A., et al., Early reduction in spectral dual-layer detector CT parameters as favorable imaging biomarkers in patients with metastatic renal cell carcinoma. *Eur Radiol*, 2022. **32**(11): p. 7323-7334.
111. Sauerbeck, J., G. Adam, and M. Meyer, Spectral CT in Oncology. *Rofo*, 2023. **195**(1): p. 21-29.
112. Das, M., et al., Carotid Plaque Analysis: Comparison of Dual-Source Computed Tomography (CT) Findings and Histopathological Correlation. *European Journal of Vascular and Endovascular Surgery*, 2009. **38**(1): p. 14-19.
113. Karlöf, E., et al., Carotid Plaque Phenotyping by Correlating Plaque Morphology from Computed Tomography Angiography with Transcriptional Profiling. *European Journal of Vascular and Endovascular Surgery*, 2021. **62**(5): p. 716-726.
114. Shami, A., et al., Atherosclerotic plaque features relevant to rupture-risk detected by clinical photon-counting CT ex vivo: a proof-of-concept study. *Eur Radiol Exp*, 2024. **8**(1): p. 14.

SPECTRAL COMPUTED TOMOGRAPHY (CT) is a diagnostic imaging modality that utilizes the energy- and material-dependence of photon attenuation to gain additional information about tissue properties. This adds another dimension to CT imaging, enabling the creation of new image types with the potential to improve the differentiation of similar tissue and detection of pathology.

The overall aim of this thesis was to evaluate the ability of spectral images, monoenergetic and material-specific images, to improve image quality and diagnostic performance in neuroradiological CT examinations.



VERONICA FRANSSON, is a medical physicist at the Department of Medical Radiation Physics at Skåne University Hospital.

